Two-phase flow simulations of fixed 3D oscillating water columns using OpenFOAM: a comparison of two methods for modeling quadratic power takeoff

Zhenhua Huang*, Shijie Huang

Department of Ocean and Resources Engineering, School of Ocean and Earth Science and Technology, University of Hawaii at Manoa, Honolulu HI, 96822, USA

Abstract

This study examines the performance of a numerical method that introduces an artificial sink term to the Reynolds-averaged Navier–Stokes equations to simulate the flow through an orifice used as a quadratic Power Takeoff (PTO) for Oscillating Water Columns (OWCs). The method replaces the quadratic PTO by an artificial Forchheimer-flow region (referred to as the artificial Forchheimer-flow method). The performance of this method was evaluated by making comparisons with the existing experimental results for two OWCs and the numerical results obtained by using air-water two-phase flow simulations of the air flow through an orifice (referred to as the orifice-flow method). The surface elevations, velocity fields and pressure fields obtained by the orifice-flow and artificial Forchheimer-flow methods are compared. To use the artificial Forchheimer-flow method, an equation for specifying the Forchheimer coefficient is provided and the sensitivity of the pneumatic efficiency to the Forchheimer coefficient is discussed. It can be concluded that the artificial Forchheimer-flow method can satisfactorily reproduce the measured pneumatic efficiency, pressure field in the air, the velocity field in the water and the cross-sectional average velocity of the air. Compared to the orifice-flow method, the artificial Forchheimer-flow method can speed up the simulation by at least 25 times.

Keywords: Wave energy, OWC, PTO, CFD, orifice, Forchheimer's law

*Corresponding author contacts:
Email address: `zhenhua@hawaii.edu` (Zhenhua Huang)

1. Introduction

Renewable energy is of great importance for a sustainable development (Falcão, 2010; Lund, 2007). Among all the renewable energy sources, wave energy stands out due to the fact that it is more predictable and has a much higher energy density compared to other renewable energy sources, such as wind or solar energy (Falcão, 2010; Chen et al., 2013).

Different types of Wave Energy Converters (WECs) have been proposed in the past to convert the wave energy into other forms of energy, such as electrical energy. One of the most widely tested and studied WECs is Oscillating Water Columns (OWCs) (Falcão, 2010; Aderinto and Li, 2018; Xu and Huang, 2019). A typical OWC device is essentially a partially submerged air chamber, which is connected to the atmosphere through a Power Takeoff (PTO) system (Aderinto and Li, 2018). A PTO system typically includes a turbine, driven by the wave-induced oscillatory air flow, and an electric generator connected to the turbine for electricity generation. One of the key characteristics of a turbine that is relevant to the power extraction efficiency is the pressure drop of the air flow through the turbine. Two main types of PTOs for OWCs have been studied in the past (Scuotto et al., 2005; Aderinto and Li, 2018): (1) linear PTOs characterized by a linear relation between the pressure drop and the mass flow rate of the air flow through a linear turbine such as a Wells turbine, and (2) quadratic PTOs characterized by a quadratic relation between the pressure drop and the mass flow rate of the air flow through a nonlinear turbine such as an impulsive turbine. The disadvantages of Wells turbines include narrow operational range, noisy operations and poor stalling characteristics (Badhurshah et al., 2018). Early studies of OWCs have focused on Wells turbines, but some recent studies of OWCs focus on impulsive turbines (Aderinto and Li, 2018).

Because of the complexity and high rotation speed of an air turbine, it is not practical to model the complex turbine aerodynamics in either small-scale model tests or numerical simulations of OWC-type WECs (Liu et al., 2016). As a result, devices other than actual turbines have been used in small-scale model tests and numerical simulations in the past to create the required pressure drop of the air flow through a turbine, which means the extraction efficiency obtained is just the pneumatic efficiency. The final efficiency of an OWC-type WEC is the pneumatic efficiency multiplied by the turbine efficiency and the generator efficiency.

Sharp-edged orifices have been widely used to model impulsive turbines in both small-scale model tests (Wang et al., 2002; Xu et al., 2016; Ning et al., 2016; He and Huang, 2017; Vyzikas et al., 2017) and numerical simulations of OWCs (Xu et al., 2016; Ahmad et al., 2018; Huang et al., 2020). Changing the opening ratio (i.e., the ratio of the area of the orifice to the cross-sectional area of the air chamber) changes the relation between the pressure drop and flow rate; therefore, the opening ratio can be used as a parameter to describe the relation between the pressure drop and the mass flow rate. It has been found that the typical opening ratio should be around 1% to achieve an optimal pneumatic efficiency (Ning et al., 2016; He and Huang, 2017). Several air-water two-phase flow models have been used to simulate the wave interaction with various OWC-type WECs where the air flow through an orifice has been used as the PTO. The small opening ratio can result in an oscillatory jet flow with a very high velocity. According to conservation of mass, the velocity of the jet flow is about 100 times faster than the velocity of the free surface fluctuation inside the chamber if the opening ratio is about 1%. Experimental studies have found that the pressure sensors mounted at different locations on the interior surface of the air chamber gave almost the same time series of the measured pressure (He et al., 2012; He and Huang, 2017).

Since the pressure inside a high-speed jet flow is expected to be approximately uniform and equal to the ambient pressures, it can be hypothesized that the air pressure inside the air chamber has negligible spatial variation even though the velocity field is not spatially uniform. This hypothesis can be easily verified by performing 3D numerical simulations of an OWC-type WEC with an orifice as its PTO. Based on the assumptions that the air pressure is spatially uniform inside the air chamber and the pressure drop across the PTO can be parameterized, theoretical analyses (Martins-Rivas and Mei, 2009; Deng et al., 2013; Zheng et al., 2020, 2019) and potential-flow-based numerical simulations (Delauré and Lewis, 2003; Ning et al., 2015) have been the two main approaches in the literature to OWC problems; both approaches are based on potential flow, and thus cannot consider viscous effects. Furthermore, theoretical approaches are suitable only for OWC WECs with simple geometries.

Air-water two-phase flow simulations of OWC-type WECS are getting more attention recently due to the rapid advances in computing technology, both in hardware and software. These simulations are based on either Reynolds-averaged Navier–Stokes (RANS) equations (Huang et al., 2019; López et al., 2014) or Large Eddy Simulation (LES)(Galera-Calero et al., 2020; Simonetti et al., 2018). However, the requirements of much finer grid and much smaller time step to simulate the high-speed flow through the orifice make the two-phase flow simulations computationally very expensive because of the requirement of Courant-Friedrichs-Lewy condition for numerical stability (Courant et al., 1967). For example, Huang et al. (2019) and Huang et al. (2020) presented three-dimensional (3D) two-phase flow simulations of a circular OWC-type WEC; they reported that about 200 wall-clock hours on Stampede2 at TACC using 160 cores were typically needed to have about 20 s of real-time results. This is the reason why most existing two-phase flow simulations of OWC-type WECs in the literature focused mainly on two-dimensional (2D) problems (Zhang et al., 2012; López et al., 2014; Kamath et al., 2015b) and only a few 3D simulations (Shalby et al., 2019; Xu and Huang, 2019) are reported in the literature. Elhanafi et al. (2017) performed both 2D and 3D simulations and found 2D simulations could overestimate the pneumatic efficiencies for high wave frequencies because of blockage effects.

In two-phase flow simulations of OWC-type WECs, the bottleneck is the small time step and fine grid required to simulate the air flow through an orifice. Even for two-phase flow simulations of 2D OWC-type WECs, about 30 wall-clock hours were needed to produce 20 s of real-time results on a workstation with 18 cores (Huang et al., 2020). For the calculation of wave energy extraction efficiency, the most important characteristics of a PTO system that need to be modeled in a simulation are: (1) the difference between the air pressures inside the air chamber and the ambient atmospheric pressure, and (2) the cross-sectional averaged velocity of the air flow inside the air chamber. The pneumatic efficiency is calculated using these two variables (Martins-Rivas and Mei, 2009; Deng et al., 2013; Xu et al., 2016).

To save on simulation time, it is appealing to have a numerical method that can capture the key features of the air flow through an orifice so that the OWC's pneumatic efficiency can be computed without the need to simulate the actual jet flow through an orifice. Attempts have been made in the past to use Darcy's law for the flow in a porous medium to simulate the air flow through a linear PTO (Luo et al., 2014; Kamath et al., 2015b,a; Anbarsooz and Faramarzi, 2016; Çelik and Altunkaynak, 2020; Gurnari et al., 2020), with the artificial Darcy-flow coefficient as a tuning parameter to be determined by matching the numerical results with the experimental results. For example, Kamath et al. (2015b) used the Darcy flow through an artificial porous layer in their simulations to represent the linear PTO studied theoretically by Sarmento and Falcão (1985) and experimentally by Sarmento (1992). They compared their simulation results with the experimental results of Morris-Thomas et al. (2007), who used an orifice plate as the PTO in the experiment; however, some differences between the measured and simulated pressures and surface velocities can be observed, most likely because the pressure drop across an orifice is not linearly related to the velocity (Crane, 1957). Recently, Çelik and Altunkaynak (2020) used a commercial software to study the resonant frequency and damping ratio of a rectangular OWC through free decay tests and compared with physical model tests where the PTOs were modeled by either the Darcy-flow through a porous media or the air flow through an abrupt contraction of a pipe; the commercial software they used is the same as that used by Mahnamfar and Altunkaynak (2017).

Attempts to use a Forchheimer flow to simulate a 3D orifice flow has not been reported in the literature. The closest work that can be found in the literature is Dimakopoulos et al. (2015), who converted a 3D circular orifice opening to a 2D rectangular slot and the 3D circular geometry of the OWC chamber to a 2D rectangular one, and filled the 2D slot with a porous media to make the slot wider, which allowed them to use a larger grid in the vicinity of the slot. Dimakopoulos et al. (2015) hypothesized that the difference between their numerical results and the experimental results for the 1.0% opening ratio was due to the compressibility of the air in the air chamber. As pointed out by He and Huang (2017), a circular opening may behave differently from a rectangular slot with the same opening ratio. Therefore, it is not clear to what extent converting the 3D geometry to a 2D one may have affected their numerical results.

Because using Darcy-flow approach to imitate flow through an orifice cannot capture the quadratic pressure drop, a key feature of the orifice flow, the motivation of this study is to verify a method for speeding up the two-phase flow simulations of OWC-type WECs with a quadratic PTO. Similar to using a Darcy flow through a porous media, the method examined here adds a sink term to the momentum equation based on Forchheimer's law which can give a quadratic pressure loss. The method is implemented using the open source CFD tool, OpenFOAM (Weller et al., 1998; Jacobsen et al., 2012). The objectives of this work are to (1) validate the method by comparing with two sets of experimental results, and (2) provide detailed comparisons of the results for a circular OWC obtained by two methods: (i) the orifice-flow method and (ii) the method using Forchheimer's law (referred to as the artificial Forchheimer-flow method to distinguish from the Darcy-flow method for linear PTOs). The comparisons focus on the pressure and velocity fields, surface elevation and pneumatic efficiency. Empirical formulas that may be used to estimate the Forchheimer coefficient in the absence of experimental data are also discussed.

2. Methods

Air-water two-phase flow simulations of two OWC-type WECs were performed using the orifice-flow method and the artificial Forchheimer-flow method to model quadratic PTOs. In both methods, both the air and water are treated as in-compressible fluids. The artificial Forchheimer-flow method adds a sink term to the momentum equation to produce a pressure drop across the artificial Forchheimer-flow region, which is approximately equal to the pressure drop caused by the air flow through an orifice. As a result, the Forchheimer-flow in this method is not the flow in a real porous media because the porosity of real porous medias is not included in the governing equations, and thus the flow in this region cannot capture the following features of porous media flows: phase saturation, relative permeability and the capillary pressure. In essence, the artificial Forchheimer-flow region is an artificial damping region designed based on the Forchheimer's law

2.1. Equations governing in-compressible air-water two-phase flows

For completeness, the two-phase flow models adopted by this study to simulate wave interaction with an OWC-type WEC are summarized here.

The in-compressible Reynolds-Averaged Navier-Stokes equations (RANS) are used to describe the flow of a water-air mixture (Rusche, 2003). A VOF method is used to track and locate the air-water interface by using a volume-fraction function s, which is the saturation of water: $s = 0$ when a cell is occupied by air alone, $s = 1$ when a cell is occupied by water alone, and $0 < s < 1$ when a cell is occupied by both the air and the water (Rusche, 2003). Anywhere in the flow, the density ρ and the dynamic viscosity μ_f are calculated by

$$\rho = s\rho_w + (1 - s)\rho_a, \tag{1}$$

$$\mu_f = s\mu_w + (1 - s)\mu_a, \tag{2}$$

where the subscripts w and a stand for water and air, respectively.

The volume-fraction function s is governed by the following transport equation:

$$\frac{\partial s}{\partial t} + \nabla \cdot [s\mathbf{u}] + \nabla \cdot [\mathbf{u}_r s(1-s)] = 0, \tag{3}$$

where $\mathbf{u}$ is the velocity of the air-water mixture. A "compression velocity" $\mathbf{u}_r$ is applied in the direction normal to the local air-water interface. The purpose of using a proper "compression velocity" is to compress the volume-fraction field and maintain a sharp air-water interface. As a rule, the "compression velocity" is determined by multiplying the maximum velocity magnitude in the computation domain by the normal vector of the air-water interface and a constant K_c. The default value of K_c is 1.5 as suggested by Rusche (2003).

The continuity and momentum equations for the in-compressible fluid are

$$\nabla \cdot \mathbf{u} = 0, \tag{4}$$

and

$$\frac{\partial \rho \mathbf{u}}{\partial t} + \nabla \cdot [\rho \mathbf{u}\mathbf{u}^T] = \rho \mathbf{g} - \nabla p + \nabla \cdot [\mu \nabla \mathbf{u}], \tag{5}$$

where $\mathbf{g}$ is the gravitational acceleration, p is the total pressure of the air-water mixture, and

$$\mu = \mu_f + \mu_t \tag{6}$$

with μ_t being the turbulent eddy viscosity, which needs to be closed by a turbulence model. The following $k - \omega$ SST turbulence model (Larsen and Fuhrman, 2018) is employed for this purpose:

$$\frac{\partial \rho k}{\partial t} + \nabla \cdot [\rho \mathbf{u} k] = \rho P_k - \rho \beta^* k \omega + \nabla \cdot [(\mu_f + \rho \sigma^* \frac{k}{\omega}) \nabla k] \tag{7}$$

$$\frac{\partial \rho \omega}{\partial t} + \nabla \cdot [\rho \mathbf{u} \omega] = \rho P_\omega - \rho \beta \omega^2 + \rho \frac{\sigma_d}{\omega} \nabla k \cdot [\nabla \omega]^T + \nabla \cdot [(\mu_f + \rho \sigma \frac{k}{\omega}) \nabla \omega] \tag{8}$$

where k and ω are specific turbulence kinetic energy and specific dissipation rate, respectively; P_k and P_ω are production terms for k and ω, respectively;

β^*, β, σ^*, σ and σ_d are model parameters. The turbulent eddy viscosity μ_t is then determined by:

$$\mu_t = \rho \nu_t, \; \nu_t = \frac{a_1 k}{max(a_1 \omega, F_2 \sqrt{S:S}, a_1 \lambda_2 \frac{\beta}{\beta^* \alpha} \frac{S:S}{p_\Omega} \omega)}, \tag{9}$$

where a_1 and λ_2 are model parameters, F_2 is a blending function that is close to 1 in boundary-layer region and 0 in free shear layers, S is the strain rate tensor defined by $S = \frac{1}{2}[\nabla \mathbf{u} + \nabla \mathbf{u}^T]$, and $p_\Omega = \nabla \times \mathbf{u}$ is 2 times the rotation tensor.

It is worth noticing that Eq. (9) is different from the original $k - \omega$ SST turbulence model in Menter (1994), where the last term in $max()$ is absent—the presence of that term can avoid the unphysical generation of turbulence energy in near potential flow regions, where $p_\Omega \ll S : S$ (Larsen and Fuhrman, 2018). The model parameters used in this paper are: $a_1 = 0.31$, $\beta^* = 0.09$, $\beta = 0.075 \sim 0.0828$, $\sigma^* = 0.5 \sim 1.0$, $\sigma = 0.5 \sim 0.856$, $\sigma_d = 0.856$, $\lambda_2 = 0.05$. The actual values of β, σ^* and σ vary within a range in the computational domain, depending on the distance of a grid to the closest wall.

2.2. The empty numerical wave tank

Based on the equations given in Section 2.1, a three-dimensional (3D) Numerical Wave Tank (NWT) was developed using OpenFOAM v1712. As shown in Fig. 1, the empty NWT consists of three sections: the Wave Generation Section (WGS), the test section and the Wave Absorbing Section (WAS). Both the wave generation and wave absorption sections are achieved using a relaxation zone method (Jacobsen et al., 2012). The relaxation zones was implemented using the library waves2Foam, which is a toolbox used to generate and absorb water waves. The length of each relaxation zone is at lest two times the maximum wave length examined in this study.

As shown in Fig. 1, the empty NWT is divided into four mesh zones: (I) the air zone; (II) the free-surface zone (or the air-water interface zone) in which the wave crests and wave troughs lie; (III) the water zone; and (IV) the two relaxation zones. The Cartesian coordinate system (x, y, z) has the x coordinate pointing in the direction of wave propagation, the y coordinate pointing vertically upward, and the z coordinate pointing out of the paper. The origin of this coordinate system is located on the still water surface and at the inlet boundary. The information of the grid for each zone is summarized in Table 1.

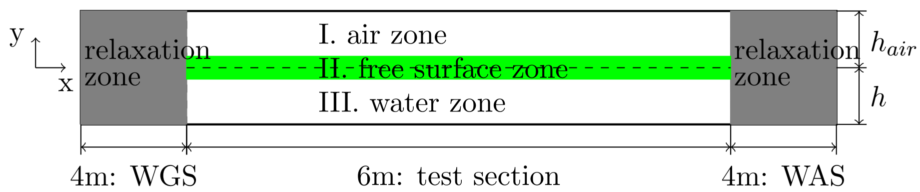

Figure 1: A sketch of the empty numerical wave tank. Not drawn to scale. The longest wave length in this study is 1.5 m.

Table 1: Information of the grids for the empty wave flume

size/zone	Zone (I)	Zone (II)	Zone (III)	Zone (IV)
Δx (cm)	1.65	1.65	1.65	1.65
Δy (cm)	1.00	0.50	1.00	1.00
Δz (cm)	5.00	5.00	5.00	5.00

Referring to Fig. 1, the height of the NWT is $h + h_{air}$, with the water depth h=0.29 m and h_{air}=0.21 m, and the total length is 14 m: 6 m for the test section, and 4 m for each relaxation zone. The width of the NWT is fixed at 0.5 m, which was the width of the wave flume in the experiment of Xu et al. (2016). Therefore, whatever side effects there might be in the physical model tests will also be present in the two-phase flow simulations[1]. The edge of the wave generation zone is at x=4.00 m and the edge of the wave absorption zone is at x=10.00 m. Problems of wave-interaction with an OWC can be studied by integrating into the grids for the test section of the NWT a set of locally-nested grids describing the geometry of the OWC as described in Section 3.1.

In a relaxation zone, the value of a variable ϕ (e.g., fluid saturation s or components of velocity $\vec{u}$) is a blend between the computed value ϕ_C and the targeted value ϕ_T with a relaxation factor β_R. Therefore, the value of ϕ in the relaxation zone can be written as

$$\phi = \beta_R \phi_C + (1 - \beta_R)\phi_T \tag{10}$$

[1]The effects of the sidewalls are expected to be small because: (1) the ratio of the flume width to the model dimension is between 4 and 5 and (2) there is no lateral waves excited by the diffraction of fundamental waves.

where the relaxation factor β_R varies in space and is specified by

$$\beta_R(X) = 1 - \frac{\exp(X^{3.5}) - 1}{\exp(1) - 1} \tag{11}$$

where $X = x'/L_R$ with x' being the distance relative to the edge of the relaxation zone and L_R the length of the relaxation zone (Jacobsen et al., 2012). For wave generation, the second order Stokes wave theory is used to provide the targeted ϕ_T; while for wave absorption, $\phi_T = 0$ is used.

Boundary conditions (BCs) at the lateral walls, the bottom of the wave flume and the OWC walls are set to be wall BCs for which the velocity is set to 0 at the boundary, ω, k and μ_t are calculated by applying wall functions, and the pressure is taken to be the same as that in the cell next to the wall. The methods to specify wall functions used here are described in Kalitzin et al. (2005). This method does not require the first cell to be in the logarithmic layer. Therefore, y^+ value varies along the boundary, depending on the flow field and the mesh used at different boundaries. The boundary condition used at the ceiling of the wave flume is the ”Pressure-inlet outlet velocity” condition provided in OpenFOAM so that the air can get in and out freely through the ceiling.

2.3. The circular OWC model with an orifice plate as a quadratic PTO

The circular OWC model shown in Fig. 2 was used to demonstrate the two methods for simulating quadratic PTOs. The OWC model consists of a C-shaped support structure, a circular OWC chamber, and a top cover which is a sharp-edged orifice plate. The OWC chamber is partially submerged with a draft D_r, and the distance between the lower tip of the OWC chamber skirt and the bed is D_s. For a given water depth h, the draft of the OWC chamber $D_r = h - D_s$. The change of quadratic PTO’s characteristics can be achieved by changing the opening ratio of the orifice plate. When the air flows through the orifice, there is a pressure drop across the orifice and the pneumatic power extracted from the wave field P_{out} is equal to the average work done by the air pressure on the water over n wave periods

$$P_{out} = \frac{1}{nT_w} \int_{t_0}^{t_0+nT_w} \left(\int \int_S p_a w_a dA \right) dt \tag{12}$$

where p_a and w_a are the air pressure and vertical velocity, respectively, S is the cross section of the air chamber on which p_a and w_a are taken, T_w is the wave period, and t_0 is an arbitrary time reference, and n is an integer.

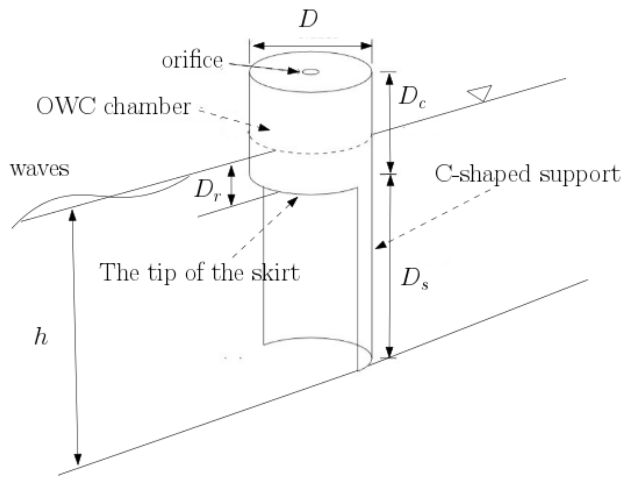

Figure 2: A sketch of the circular OWC model.

The pneumatic efficiency of the OWC-type WEC ϵ is defined by the ratio of the so-called capture width λ to the chamber diameter D_{OWC}.

$$\epsilon = \frac{\lambda}{D_{OWC}}, \qquad \lambda = \frac{P_{out}}{P_i} \tag{13}$$

where P_i is the wave power per unit wave crest in the incident waves. For second Stokes waves in water of depth h

$$P_i = ECn(1 + (kA_i)^2\xi) \tag{14}$$

$$E = \frac{1}{2}\rho_w g A_i^2, C = \frac{\omega}{k}, n = \frac{1}{2}\left(1 + \frac{2kh}{\sinh(2kh)}\right) \tag{15}$$

$$\xi = \frac{9}{8n}\frac{\cosh(kh)}{\sinh^7(kh)}\left[\frac{\sinh(4kh) + 4kh}{8\sinh^2(kh)} - \frac{\sinh(2kh)}{6}\right] \tag{16}$$

where A_i is the amplitude of the first harmonic, $\omega = 2\pi/T_w$, k is the wave number, ρ_w is the density of water, and g is the gravitational acceleration. The contribution from the second harmonic wave is small for the present problem (less than 1%).

The model shown in Fig. 2 has been studied experimentally by Xu et al. (2016), who also extended the linear potential-flow theory of Deng et al. (2013) by including a quasi-linear PTO model to calculate the power extraction by an orifice. In the experiment of Xu et al. (2016), the circular orifice had a diameter of 0.014± 0.0002 m. The inner diameter of the OWC chamber D was 0.125$\pm$ 0.0005 m, and the thickness of the wall was 0.003 m. The uncertainties in the diameter of the opening and the diameter of the OWC chamber were estimated based on multiple measurements along different directions. From the sizes of the opening and the OWC chamber, the opening ratio α is in the range of 1.210% and 1.300%, with an average value of 1.255%, i.e., $\alpha = (1.255 \pm 0.045)\%$. The distance from the lower tip of the OWC chamber to the bed D_s was 0.25 m, and the overall height of the OWC model was 0.4 m. Two water depths were examined in Xu et al. (2016), and h=0.29 m was used in this study for comparing the results obtained by the two methods for simulating the quadratic PTO (i.e., the orifice plate in the experiment).

2.4. The orifice-flow method

In their OpenFOAM-based, three-dimensional (3D) two-phase flow simulations of the OWC shown in Fig. 2, Huang et al. (2019), Xu and Huang (2019) and Huang et al. (2020) simulated the air flow through the orifice to obtain the characteristics of the quadratic PTO. Because of the small size of the opening and the thin wall in the OWC model, meshes much finer than the meshes used for the empty flume are needed adjacent to the wall and in the vicinity of the opening. For example, the smallest mesh generated by using *snappyHexMesh* to fit the OWC model in Xu and Huang (2019) has the following dimensions: 0.001 m x 0.001m x 0.001 m, which was based on a mesh convergence study (See Appendix B). To achieve a balance between the computational cost and accuracy in this study, the smallest mesh generated by using *snappyHexMesh* to fit the OWC model has the following dimensions: 0.00125 m x 0.0015 m x 0.00125 m. For the test conditions examined by Xu et al. (2016) and Xu and Huang (2019), the speed of the air flow through the orifice was greater than 10 m/s in the experiment. For a stable numerical simulation, the Courant–Friedrichs–Lewy (CFL) condition requires that the following Courant number must be smaller than unity

$$C = \Delta t \left(\sum_{j=1}^{3} \frac{u_j}{\Delta x_j} \right) \tag{17}$$

where u_j is the magnitude of the $j-$th velocity component, Δx_j is the grid size of the $j-$th coordinate, Δt is the time step. Xu and Huang (2019) and Huang et al. (2020) found that the Courant number must be around 0.4 in general (sometimes a value of 0.2 was needed to march the simulation for several time steps) to achieve numerical stability [2]. The combination of high speed, small mesh size and small Courant number results in very small time steps and very long time to run the simulation, which makes it impossible to run the simulation on PC or a single workstation. The simulations reported in Xu and Huang (2019) and Huang et al. (2020) were performed on Stampede2 at TACC using 160 cores, and 200 wall-clock hours were typically needed for about 20 s of numerical results. Therefore, simulating the high-speed air flow through a small orifice is the bottleneck in the two-phase flow simulations of OWCs with an orifice as the PTO.

2.5. Pressure drop across an orifice

Both physical experiments (Xu et al., 2016; He and Huang, 2017) and CFD simulations of the air flow through an orifice using the orifice-flow method (Xu and Huang, 2019; Huang et al., 2020) have found that the following expression can describe the pressure drop across an orifice plate well:

$$\tilde{p}_{in} - \tilde{p}_{out} = \frac{1}{2} C_f \rho |\langle w \rangle| \langle w \rangle + L_\alpha \rho \frac{\partial \langle w \rangle}{\partial t}, \tag{18}$$

where $\tilde{p}_{in}$ and $\tilde{p}_{out}$ are the dynamic pressures inside and outside the air chamber, respectively, $\langle w \rangle$ is the cross-sectional averaged vertical velocity of the air flow inside the air chamber, and C_f and L_α are two parameters determined by either experiments or numerical simulations. The dynamic pressure outside the air chamber $\tilde{p}_{out}$ can be set to approximately zero. The last term in Eq. (18) represents the effect of the flow inertia on the pressure drop.

For the change of hydrodynamic pressure induced by long water waves passing through a perforated plate, Mei (1992) derived an expression similar to Eq. (18). Unlike in long water waves passing through a perforated plate where the flow pattern for the water moving forward is a mirror image of that for the water moving backward, the air inhalation and exhalation processes are slightly different, as shown in Appendix A. This is because the air flow outside the OWC chamber is not confined laterally by any boundary, while the air flow inside the air chamber is confined by the wall of the air chamber.

[2]The computations were performed using multiple nodes on a high-performance computing facility. The communication between nodes sometimes may cause numerical instability. This instability issue is hardware- and software-dependent. When this type of numerical instability occurs, our experience is that it may be overcome by marching the simulation for several time steps with a smaller Courant number.

Nevertheless, both the existing experimental studies (Xu et al., 2016; He and Huang, 2017) and CFD simulations of the air flow through an orifice using the orifice-flow method (Huang et al., 2019, 2020) have shown that the inertia term in Eq. (18) is much smaller than the quadratic loss term for the present problem and Eq. (18) can provide an adequate description of the air pressure drop across an orifice with a constant C_f (see Appendix A).

2.6. Parameterization of the orifice flow by an artificial Forchheimer flow

Mathematically, the quadratic PTO can be represented by the energy loss associated with a quadratic pressure drop between the air chamber and the ambient air, which makes it possible to use an artificial Forchheimer flow to model a quadratic PTO.

Even though the flows during the inhalation and exhalation periods are not exactly the same as shown in Appendix A, the value of C_f for the inhalation period is only slightly different from that for the exhalation period: the two values of C_f deviate from its mean only by about 7% for the circular OWC model shown in Fig. 2. In the following, a constant C_f will be assumed.

2.6.1. Equations for artificial Forchheimer flow

OpenFOAM allows users to include in Eq. (5) an empirical sink term $\mathbf{S}_m$, i.e.,

$$\frac{\partial \rho \mathbf{u}}{\partial t} + \nabla \cdot [\rho \mathbf{u}\mathbf{u}^T] = \rho \mathbf{g} - \nabla p + \nabla \cdot [\mu \nabla \mathbf{u}] + \mathbf{S}_m, \tag{19}$$

For the sink term $\mathbf{S}_m$, Darcy-Forchheimer model is one of the models that the user can choose from by setting OpenFOAM's *fvOptions* file in the *system* folder for the problem. It is stressed that this model employs the porous media analogy but sets the porosity of the porous media to 1. For a homogeneous porous media the following Darcy-Forchheimer equation can be used to model the sink term

$$\mathbf{S}_m = -\left[\mu_f \beta_D + \frac{1}{2}\rho f\,|\mathbf{u}|\right]\mathbf{u} \tag{20}$$

where β_D is a constant Darcy's resistance coefficient and f is a constant Forchheimer coefficient having a unit of m^{-1}, and both are scalar model parameters for the homogeneous porous media. Since the porosity is set to unity, the model cannot simulate features such as phase saturation, relative permeability and the capillary pressure. It is because of this reason, the method using Eq. (20) to imitate an orifice plate is referred to an artificial Forchheimer-flow method in this study to avoid confusion with the real flow in a porous medium.

It is remarked that Dimakopoulos et al. (2015) used a different momentum equation, which includes the porosity in their momentum equation for the flow in their porous layer, but their expression for the sink term is formally the same as Eq. (20).

2.6.2. Assumptions behind the artificial Forchheimer flow method

Next we show that using Eq. (20) can produce the quadratic pressure drop across the orifice plate given by Eq. (18) by establishing a relationship between the model parameter f in Eq. (20) and the quadratic loss coefficient of an orifice C_f in Eq.(18).

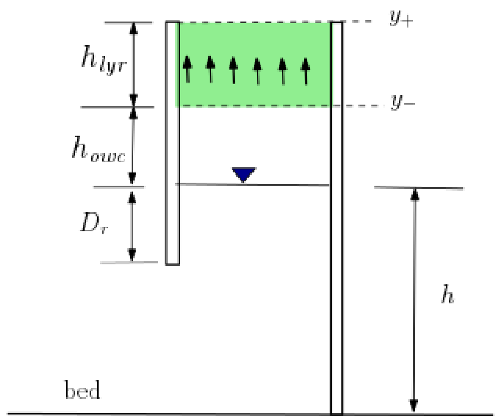

Figure 3: The orifice plate is replaced by an artificial Forchheimer-flow region of a thickness h_{lyr}.

Referring to Fig. 3, the orifice plate is replaced by a region occupied by an artificial Forchheimer-flow region, which is bounded by the OWC wall, the planes of $y = y_-$ and $y = y_+$. The thickness of this region is h_{lyr}. To proceed, we assume that

(i) The pressures on the two sides of the orifice plate are almost uniform.
(ii) The artificial Forchheimer flow is almost parallel to the chamber walls and spatially uniform except in the boundary layer adjacent to the wall.
(iii) Both the orifice-flow method and artificial Forchheimer-flow method give the same the cross-sectional average of the vertical velocity.

(iv) The Reynolds stress is not important in the artificial Forchheimer-flow region.

It will be shown later that the first assumption can be verified by the results obtained by using the orifice-flow method. The second and third assumptions lead to $w \approx \langle w \rangle$, where $\langle . \rangle$ stands for taking cross-sectional average of its argument, and make the values of $\langle w \rangle$ obtained by the two numerical methods to be approximately the same. As a result, Eq. (19), which governs this artificial Forchheimer flow, can be approximately written as

$$\frac{\partial \rho \langle w \rangle}{\partial t} \approx -\frac{\partial \tilde{p}}{\partial y} + S_m, \tag{21}$$

where $\tilde{p} = p + \rho g y$ is the dynamic pressure, w is the velocity in y-direction and the source term S_m is given by

$$S_m = -\left[\mu_f \beta_D + \frac{1}{2}\rho f \left|\langle w \rangle\right|\right] \langle w \rangle. \tag{22}$$

Integrating Eq. (21) from y_- to y_+ gives

$$h_{lyr} \frac{\partial \rho \langle w \rangle}{\partial t} \approx -(\tilde{p}_{out} - \tilde{p}_{in}) + S_m h_{lyr}, \tag{23}$$

where h_{lyr} is the thickness of this artificial Forchheimer-flow region. Comparing Eq. (23) and Eq. (18) and taking $\beta_D = 0$ in Eq. (22) gives

$$f = \frac{C_f}{h_{lyr}},\ L_\alpha = h_{lyr}. \tag{24}$$

Previous studies (Xu et al., 2016; He and Huang, 2017; Huang et al., 2019, 2020) have shown that the inertia term in Eq. (18) is not important (See also Appendix A); therefore, it is expected that the results should not be sensitive to the thickness of the artificial Forchheimer-flow region h_{lyr} .

2.6.3. Summary

In order to use the artificial Forchheimer-flow method to model quadratic PTOs, the four assumptions listed in Section 2.6.2 must be met and the Forchheimer coefficient should be determined by $f = C_f/h_{lyr}$.

3. Results

The performance of the artificial Forchheimer-flow method is evaluated in this section by comparing with both experimental results and the numerical results obtained by using the orifice-flow method. In addition to the circular OWC shown in Fig. 2, which has an opening ratio fixed at 1.25%, the rectangular OWC studied experimentally by He and Huang (2017), which has an opening ratio varying in the range of 0.635% and 1.875%, is also used to validate the artificial Forchheimer-flow method.

All simulations were run on Stampede2 at TACC using 160 cores. For the circular OWC which has a wall thickness of 0.003 m, simulations using the orifice-flow method typically took 200 wall-clock hours to obtain about 20 s of numerical results, while simulations using the artificial Forchheimer-flow method took only about 8 wall-clock hours [3]. Therefore, the artificial Forchheimer-flow method can speed up the simulation by a factor of about 25.

3.1. The circular OWC in Xu et al. (2016)

To use the orifice-flow method to simulate the air flow through the orifice used as the PTO of the circular OWC shown in Fig. 2, a set of nested grids shown in Fig. 4 are integrated into the grids for the empty NWT to represent the geometry of the OWC model. The information of the nested grids representing the geometry of the circular OWC is summarized in Table 2, where BG_1 and BG_2 are the background grids for the empty flume. The grid G_1 provides a transition from BG_1 and BG_2 to the inner grid G_2. The integration of the grids G_1 and G_2 into the background grids BG_1 and BG_2 for the empty tank is achieved by using the OpenFOAM's built-in mesh utilities *refineMesh* and *snappyHexMesh*. During the grid refinement, an inner most mesh with a multiplayer configuration inside the grid G_2 is automatically generated to capture more geometrical details of the OWC model and improve the mesh quality. In the present study, *snappyHexMesh* generates a mesh with a two layer configuration: the first layer has a thickness of 0.5

[3] Çelik and Altunkaynak (2020) reported that a computation time ranging from 24 to 36 hrs wall-clocktime was needed to obtain about 8s simulation in their simulation of 3D free decay tests. It is not clear how many grids, what computing facility and how many cores they used in their studies. Their Fig. 5 shows the mesh used in their study; it seems their mesh is much coarser than ours

times the size of G_2 grid and the second layer has a thickness of 1.2 times the thickness of the first layer.

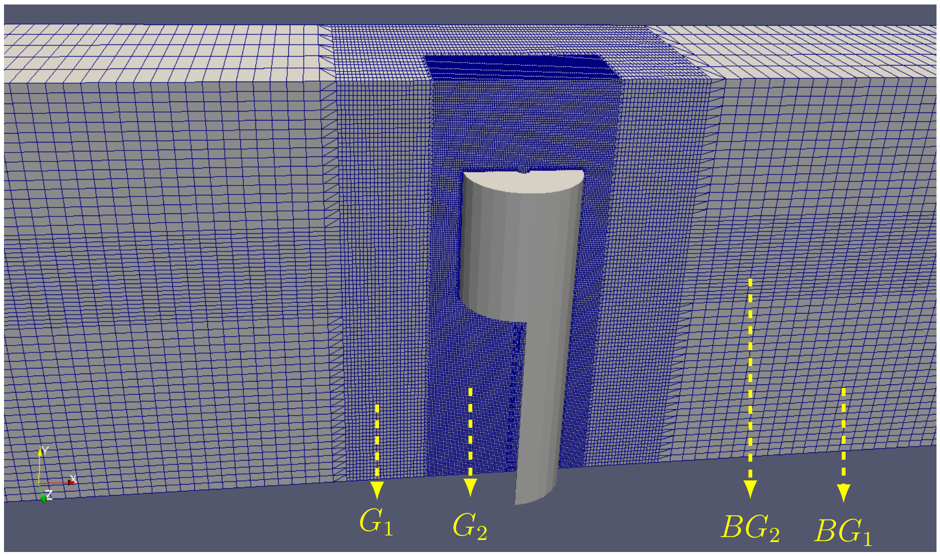

Figure 4: The nested grids for the circular OWC with an orifice plate. Grids generated by using *snappyHexMesh* are not labeled in the figure.

Table 2: Grids for the circular OWC model

size/zone	BG_2	BG_2	G_1	G_2
Δx (cm)	1.65	1.65	0.41	0.21
Δy (cm)	1.00	0.50	0.50	0.25
Δz (cm)	5.00	5.00	1.25	0.31

To evaluate the performance of the artificial Forchheimer-flow method, the pressure loss coefficient C_f obtained by using the orifice-flow method was used to determine the Forchheimer coefficient f using Eq. (24) for a given thickness h_{lyr}. As will be shown in Section 3.5, several thicknesses have been examined, and the results have confirmed that the simulated pressure drop and pneumatic efficiency are not sensitive to the thickness of the artificial Forchheimer-flow region. In all examples presented hereinafter, h_{lyr}=0.05 m was adopted, and the grid in the artificial Forchheimer-flow region is the same as the grid G2: Δx=0.0021 m, Δy=0.0025 m and Δz=0.0031 m.

Results presented in Section 3.1 are for two wave periods: T=1.2 s and T=0.8 s. The C_f value used to determine the Forchheimer coefficients f by

Eq. (24) is C_f=1.40 $\times 10^4$, which was determined by using the pressure and surface elevation provided by the orifice-flow method. It is believed that the surface non-uniformity inside the OWC chamber does not have a significant influence on the determined C_f value for this relative long period wave (Xu and Huang, 2019).

3.1.1. Air pressure and surface elevation

First we examine the results for the test condition "GP1f" in Xu et al. (2016): wave period=1.2 s, wave height=0.037 m and water depth=0.29 m. The measured and simulated air pressures and surface elevations inside the chamber are compared in Fig. 5, where the results obtained using the orifice-flow method are labeled as "orifice", the results obtained using the artificial Forchheimer-flow method are labeled as "Forchheimer", and the results obtained from the physical model test reported in Xu et al. (2016) are labeled as "experiment". It can be seen from the comparison that the time series of the air pressures and surface evaluations given by the two numerical methods are nearly identical and both agree well with the experimental results.

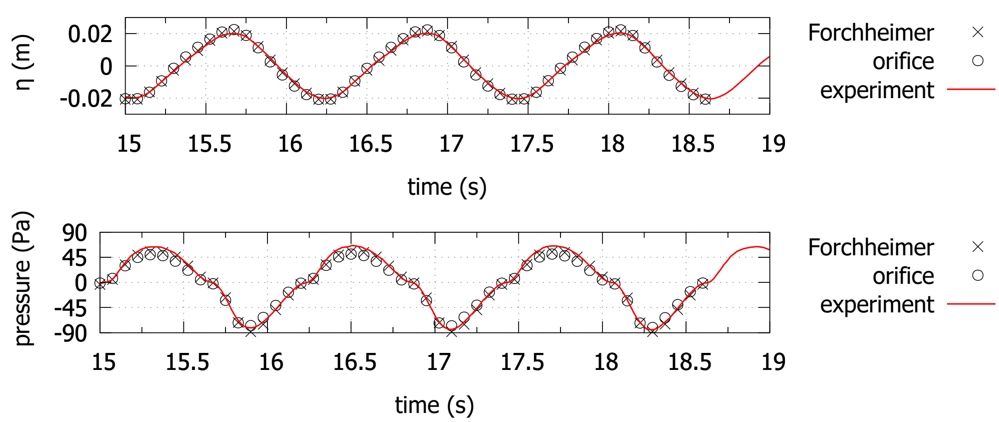

Figure 5: Time series of the surface elevation at one point (top) and the air pressure at one point (bottom) for wave period=1.2 s, wave height=0.037 m and water depth=0.29 m.

It is remarked that as in the experiment, the numerical wave gauges used in the CFD simulations (both the orifice-flow method and the artificial-Forchheimer flow method) are located at the location 0.037 m away from the center axis of the OWC chamber in the down-wave direction. The pressure sensor in the numerical simulation is located at a grid nearest to the location where the pressure sensor was mounted in the experiment (on the top of the OWC chamber, 0.05 m cm from the orifice center in the up-wave direction). As will be shown by our numerical results, the pressure distribution in the air chamber is almost uniform; therefore, the exact location of the pressure sensor is immaterial.

Next we examine the results for the test condition "GP1b" in Xu et al. (2016): wave period=0.8 s, wave height=0.037 m and water depth=0.29 m. The measured and simulated air pressures and surface elevations inside the chamber are compared in Fig.6. Again, the numerical results obtained using the artificial Forchheimer-flow method agree well with the experimental results.

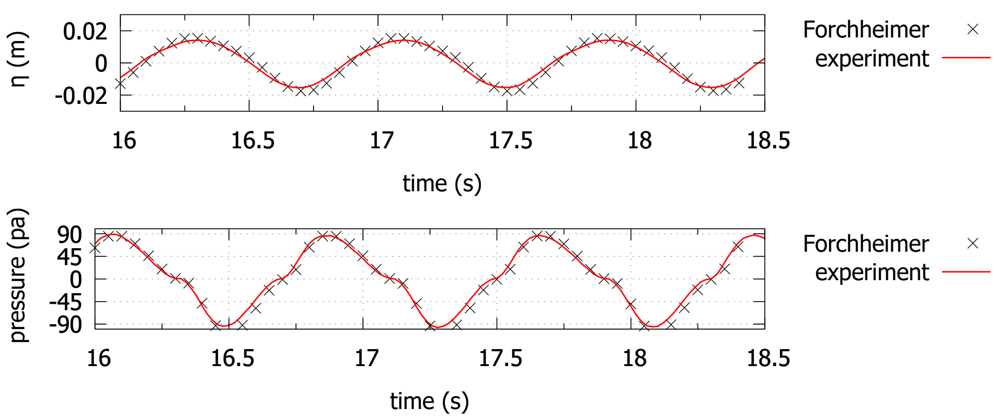

Figure 6: Time series of the surface elevation at one point (top) and the air pressure at one point (bottom) for wave period=0.8 s, wave height=0.037 m and water depth=0.29 m.

It can be concluded that the artificial Forchheimer-flow method and the orifice-flow method can produce almost the same surface elevation and air pressure inside the OWC chamber. It is remarked that in either the orifice-flow method or the artificial Forchheimer-flow method, C_f is not a turning parameter.

3.1.2. Velocity field of the air flow

It has been assumed in Section 2.6.2 that the artificial Forchheimer-flow is almost uniform spatially, which is approximately equal to the cross-section average of the velocity obtained by using the orifice-flow method. These assumptions can be verified by comparing the velocity fields of the air flow obtained by the two numerical methods.

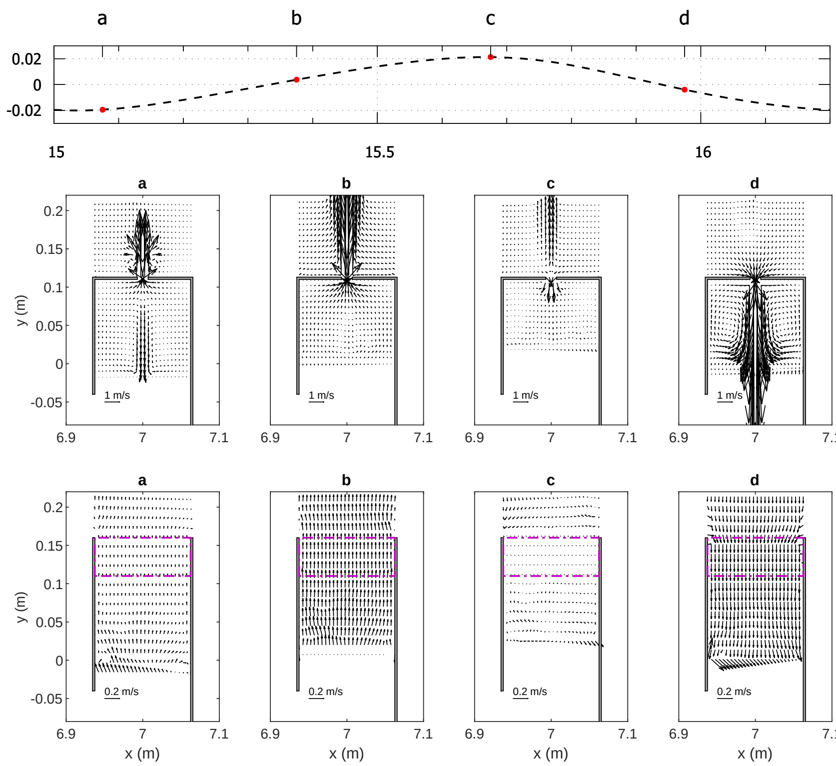

Figure 7: A comparison of the air velocity fields obtained by the two method. The four snapshots are taken in the plane of symmetry within one period. The dashed boxes in the bottom row indicate the artificial Forchheimer-flow region. The arrow in each plot denotes the scale of the velocity vectors.

Four snapshots of the velocity fields for the air flow in the plane of symmetry are shown in Fig. 7, which compares the velocity fields obtained using the artificial Forchheimer-flow method with those obtained using the orifice-flow method. The velocity fields obtained by these two methods look very different.

For the velocity field obtained by using the orifice-flow method, a jet flow exists during both the air exhalation and inhalation periods. The maximum velocity in the jet is as high as 10 m/s. For velocity field obtained by the artificial Forchheimer-flow method, the air flow indeed is almost uniform spa-

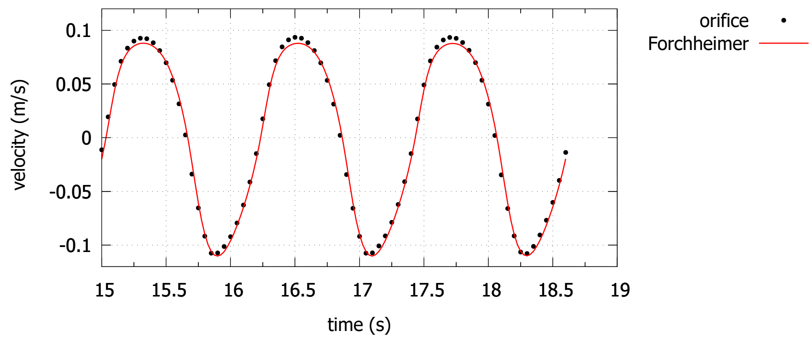

Figure 8: Time series of volume flux obtained by using the orifice-flow method (labeled as "orifice") and the artificial Forchheimer flow method (labelled as "Forchheimer").

tially in the artificial Forchheimer-flow region. The air flow is also almost uniform spatially in the air chamber, except very close to the air-water interface where the velocity is determined by the motion of the water surface. These results can verify the second assumption made in Section 2.6.2.

Fig. 8 shows a comparison between the time series of the velocities averaged over the cross section of the air chamber, obtained by the two numerical methods. Even though the velocity fields obtained by the two numerical methods look very different, the velocities averaged over the cross section of the air chamber are almost the same, which verifies the third assumption made in Section 2.6.2.

3.1.3. Pressure fields of the air

The first assumption in Section 2.6.2 is about the pressure on either side of the orifice plate. Fig. 9 shows the pressure fields of the air flow obtained by using both methods. It can be seen that the pressure on either side of the orifice plate is approximately uniform, even through the velocity field shows the existence of jet flows.

The pressures on the top and bottom of the the artificial Forchheimer-flow region are also practically uniform. Instead of a sudden jump in the pressure across the thin orifice plate, the pressure in the artificial Forchheimer-flow is almost uniform on any plane of a constant y, and the pressure changes gradually from the pressure inside the air chamber to the atmospheric pressure outside the air chamber. In other words, the artificial Forchheimer-flow method only distributes the pressure jump across the orifice plate over the thickness of the artificial Forchheimer-flow region, but keeps the air pressure

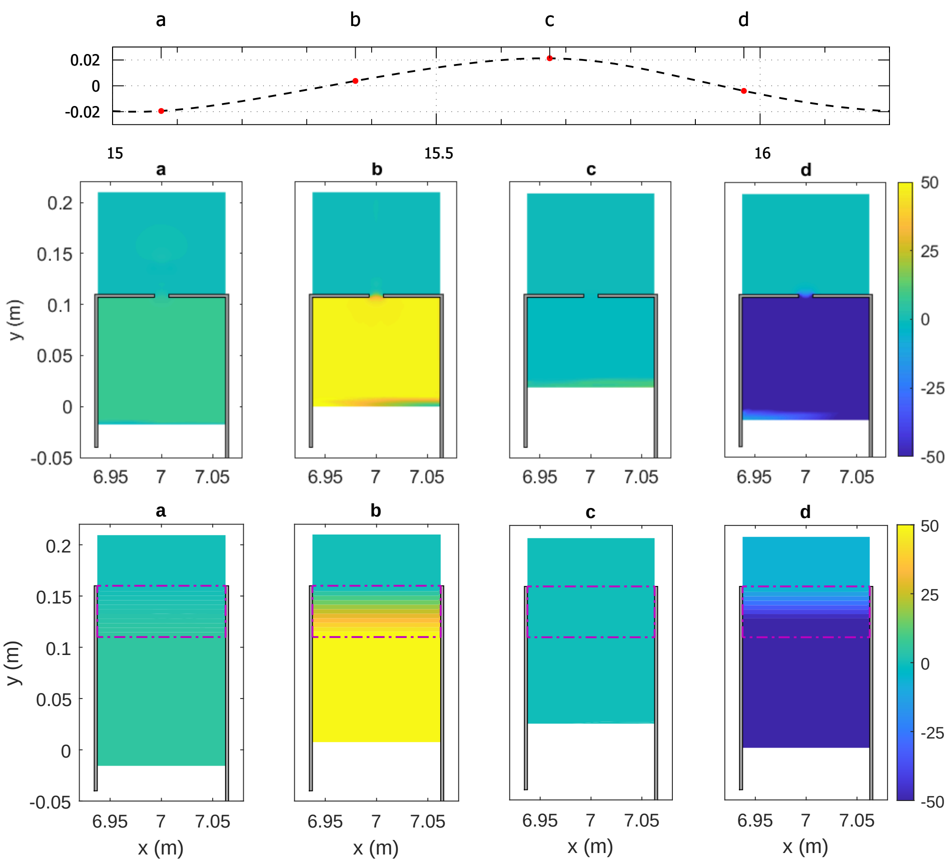

Figure 9: A comparison of the pressure fields obtained by the two methods. These snapshots are taken in the plane of symmetry within one period. The dashed boxes in the bottom row indicate the artificial Forchheimer-flow regions.

inside the chamber the same as that for the orifice flow. Therefore, it can be concluded that the first assumption made in Section 2.6.2 can be verified by the simulated pressure fields.

3.1.4. Velocity field around of the skirt of the OWC chamber

The flow pattern around the skirt of the OWC chamber is directly related to the energy loss due to vortex shedding (Xu et al., 2016). Huang et al. (2020) have been shown that the orifice-flow method used here can reproduce the velocity fields of the water flow measured by López et al. (2015) for a 2D OWC. Fig. 10 shows four snapshots of the velocity field of the water flow in the plane of symmetry. It can be seen by comparing the results obtained by the two methods that the artificial Forchheimer-flow method can capture the main features of the water flow around the OWC chamber skirt well. However, minor differences do exist, especially at the phase "a" and phase "d". A discussion of the minor differences in the velocity fields obtained by the two methods is provided in Section 4.2 .

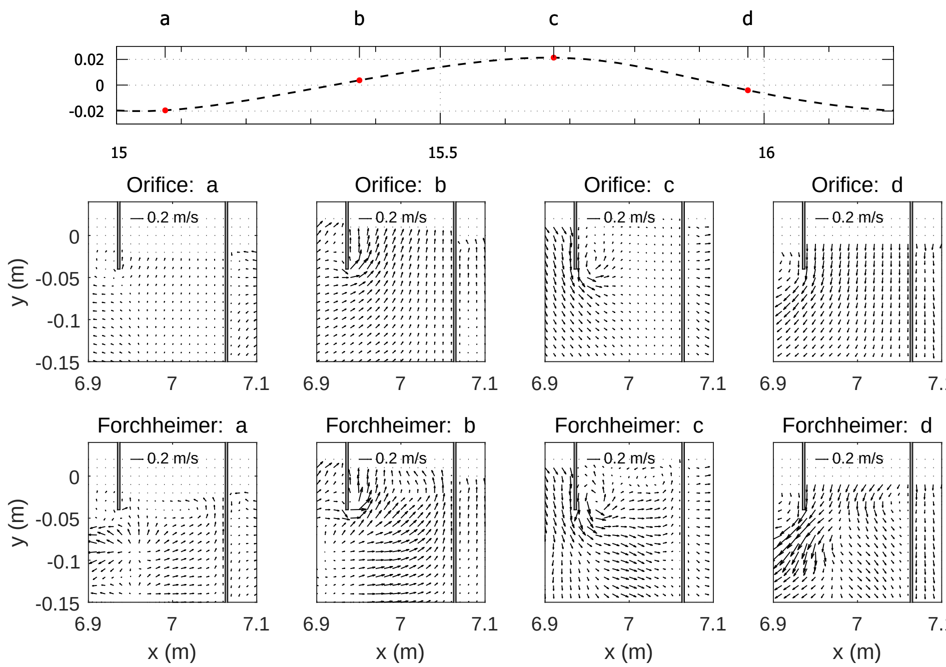

Figure 10: A comparison of the velocity fields obtained by two methods. The four snapshots are taken in the plane of symmetry within one period. Top panels for the orifice flow method and the bottom panels for the artificial Forchheimer-flow method.

3.1.5. Velocity field in horizontal planes

The velocity field close to the bed affect the sediment transport and local sour around the OWC WEC (Huang et al., 2020). Fig. 11 shows four snapshots of the velocity field of the water flow in the horizontal plane located at 0.1 m above the bed. The mean flow fields in the last column were calculated by averaging the velocity fields within three wave periods. It can be concluded that the artificial Forchheimer-flow method can capture the key features of the flow fields well in this plane, except for some minor differences.

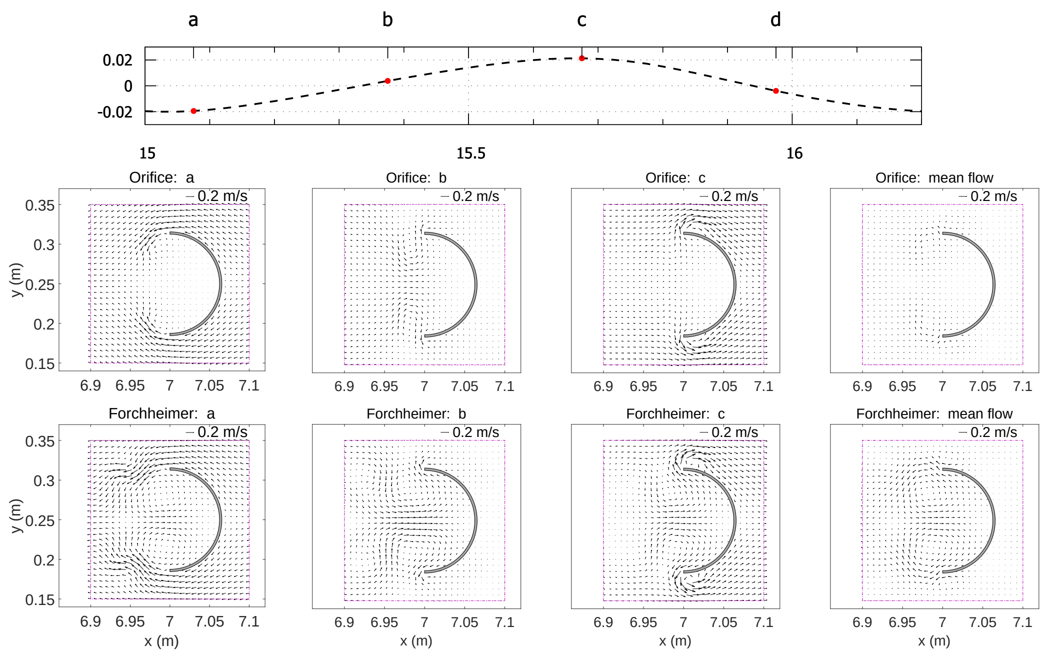

Figure 11: A comparison of the velocity fields in a horizontal plane located at 0.1 m above the bed. The top row is for the orifice flow and the bottom for the artificial Forchheimer-flow. The first three columns are for instantaneous flow fields and the last column is for the mean flow field.

Fig. 12 shows four snapshots of the velocity field of the water flow in the horizontal plane located at 0.005 m above the bed. Again the mean flow fields in the last column were calculated by averaging the velocity fields within three wave periods. The near-bed flow pattern is responsible for local scour around the OWC WEC (Huang et al., 2020). It can be concluded that the artificial Forchheimer-flow method can capture the key features of the instantaneous as well as the mean flow field well in this plane.

3.2. The rectangular OWC in He and Huang (2017)

He and Huang (2017) studied the effects of orifice characteristics on the performance of a rectangular OWC. The OWC's PTO was modelled using either a circular orifice and a narrow slot. Three opening ratios were examined: 0.625%, 1.250% and 1.875%. Six sets of their experimental results for circular orifices were used here to evaluate the performance of the artificial Forchheimer-flow method. The purpose is to demonstrate that the artificial Forchheimer-flow method can be applied to different opening ratios and

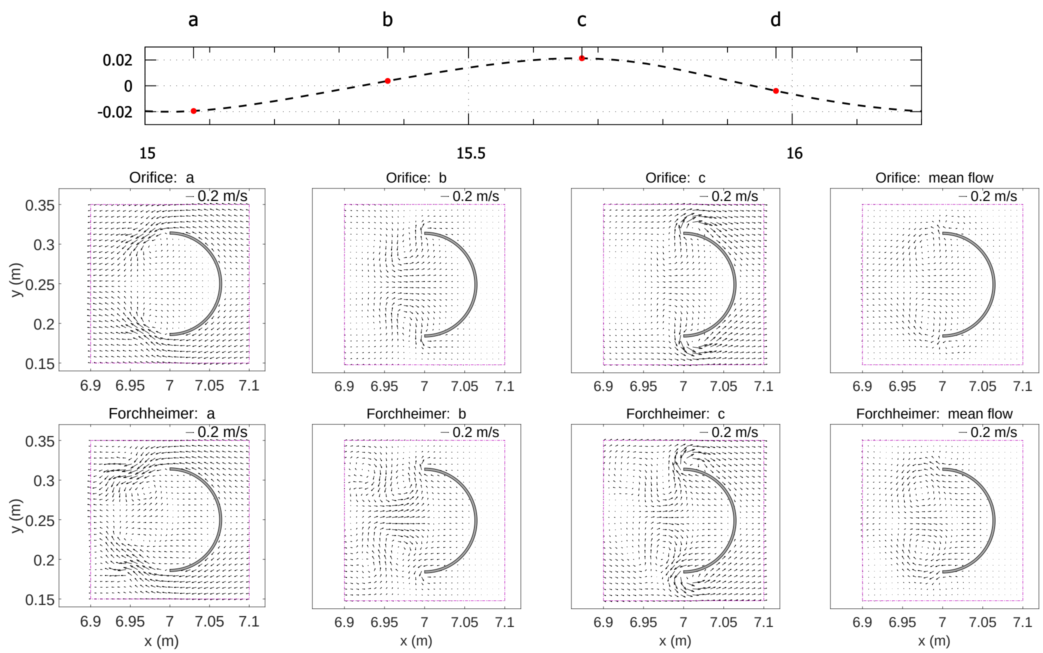

Figure 12: A comparison of the velocity fields in a horizontal plane located at 0.005 m above the bed. The top row is for the orifice flow and the bottom for the artificial Forchheimer-flow. The first three columns are for instantaneous flow fields and the last column is for the mean flow field.

different shapes of OWCs. The demonstration was done under two wave conditions: (i) wave period=1.5 s, water depth=0.4 m and wave height=0.035 m; (ii) wave period=1.0s, water depth=0.4 m and wave height=0.035 m. The orifice plate is replaced by an artificial Forchheimer-flow region, which is 0.1 m thick and placed at 0.2 m above the still water level. The value of Forchheimer coefficient f for each opening ratio is determined using Eq. (24) with the values of C_f reported in He and Huang (2017). Since the thickness of the chamber walls used in the experiment was 0.01 m, it took only about 3 hours to obtain 25 s of numerical results on the TACC's Stampede2 using 160 cores.

He and Huang (2017) reported their results in terms of pneumatic efficiency ϵ, amplification factor C_a and pressure coefficient C_p. The pressure coefficient C_p and the amplification factor C_a are defined by

$$C_p = \frac{\Delta p}{\rho_w g H_i}, C_a = \frac{\Delta \eta}{H_i}, \tag{25}$$

where Δp is the difference between the maximum and minimum values of the air pressure inside the air chamber, $\Delta\eta$ is the difference between the maximum and minimum values of the cross-sectional average of the surface elevation inside the chamber, H_i is the incident wave height, and ρ_w is the water density. The pneumatic efficiency ϵ has been defined in Eq. (13).

The comparison between the numerical and experimental results (C_a, C_p and ϵ) are summarized in Table 3 for T=1.5 s and in Table 4 for T=1.0 s. In these two tables, the first number in the pair (n_1, n_2, n_3) is the value reported in He and Huang (2017), the second is the value obtained by using the artificial Forchheimer-flow method, and the third number is the relative difference defined by $n_3 = (n_2 - n_1)/n_1 \times 100$.

Table 3: Comparisons of the measured and simulated C_p, C_a and ϵ for $T = 1.5$ s.

α	C_p	C_a	ϵ
0.625%	0.454, 0.418, -7.9%	0.574, 0.670, 16.7%	0.301, 0.295, -2.0%
1.250%	0.218, 0.207, -5.1%	0.858, 0.906, 5.6%	0.202, 0.202, 0%
1.875%	0.125, 0.111, -1.1%	0.942, 0.997, 5.84%	0.119, 0.113, -5.1%

Table 4: Comparisons of the measured and simulated C_p, C_a and ϵ for $T = 1.0$ s.

α	C_p	C_a	ϵ
0.625%	0.403, 0.365, -9.4%	0.399, 0.423, 6.0%	0.338, 0.353, 4.4%
1.250%	0.249, 0.228, -8.4%	0.672, 0.650, -3.3%	0.370, 0.341, -7.8%
1.875%	0.163, 0.147, -9.8%	0.812, 0.779, -4.0%	0.302, 0.265, -12.3%

For the case of T=1.5 s, the difference between the measured and simulated pneumatic efficiency is less than 0.01 for all three opening ratios , with the relative difference being less than 5% (less than 2.0% for α=0.625%, which provide the best pneumatic efficiency). The relative difference between the measured and simulated C_p is less than 8%, possibly because a constant C_f is used for both the inhalation and exhalation processes. The relative difference between the measured and simulated C_a is about 5% except for the smallest opening ratio, which has a relative difference of 16.7%, possibly due to the fact that the value of C_a for α=0.625% is a bit abnormal in the experiment. Nevertheless, the relative difference between the simulated and measured C_a does not significantly affect the pneumatic efficiency because when the cross-sectional average of the surface displacement is at either a crest or a trough the average velocity is zero and thus the instantaneous power extraction is also zero at that instant.

For the case of T=1.0 s, the simulated C_p is always about 9% smaller than the measurement, which again is due possibly to the use of a constant C_f in the simulation for both the inhalation and exhalation processes. The relative difference between the simulated and measured C_a is less than 6% for all three opening ratios. The relative difference between the simulated and measured efficiency increases with increasing opening ratio. Even though the largest relative difference between the simulated and measured efficiencies is about 12% for the largest opening ratio which has the lowest pneumatic efficiency, but the absolute difference between the simulated and measured efficiencies is less than 0.04 for all three opening ratios. The large relative difference for shorter waves might be due to the strong non-uniformity of the surface displacement inside the OWC chamber, which can be caused by sloshing waves or a slight non-normal incidence in the experiment. Sloshing waves standing waves which can be excited by vortex shedding (Zhao et al., 2014; Xu and Huang, 2019). The effect of non-normal incidence for longer waves is expected to be less important compared to shorter waves.

It is remarked that the difference between the simulated and measured pneumatic efficiencies is not due to the air impressibility in the model tests, as argued in Section 4.3. It can be concluded that the artificial Forchheimer-flow method can provide all important key parameters for OWCs in reasonable agreement with the measurement for different wave periods and opening ratios.

3.3. Determination of the quadratic loss coefficient C_f for circular orifices

To use the artificial Forchheimer-flow method to speed up the simulation of wave-interaction with an OWC with an orifice plate as the quadratic PTO, it is desirable to have a way to provide the value of C_f for a given orifice plate, without doing either physical model tests or performing simulations using the orifice-flow method. For the flow of an in-compressible fluid through a sharp-edged orifice in a pipe, the following two empirical formulas can be used to estimate the quadratic loss coefficient C_f:

1. The formula of Crane (1957), which was proposed for steady flow through a sharp-edged orifice in a pipe.

$$C_f = \begin{cases} [2.72 + \alpha\,(120/Re - 1)]\,[1-\alpha]\,[1/\alpha^2 - 1]\,, & Re \leq 2500 \\ [2.72 + \alpha(4000/Re)]\,[1-\alpha]\,[1/\alpha^2 - 1]\,, & Re > 2500 \end{cases} \tag{26}$$

where α is the opening ratio for a sharp-edged circular orifice in a pipe and the Reynolds number is defined by $Re = D\langle w\rangle/\nu$, where D is the inner diameter of the pipe, ν the kinematic viscosity of the air, and $\langle w\rangle$ the cross-sectional average of the air velocity in the chamber.

2. The formula of Mei (1992), which was derived for the loss of hydrodynamic pressure caused by long water waves through a vertical perforated plate with sharp-edged holes.

$$C_f = \left(\frac{1}{\alpha C_c} - 1\right)^2. \tag{27}$$

For circular, sharp-edged orifices, the discharge coefficient C_c can be determined by the following well-known Chisholm expression (Fossa and Guglielmini, 2002):

$$C_c = \frac{1}{0.639(1-\alpha)^{0.5} + 1} \tag{28}$$

It is remarked that the expression for C_f given by Eqs. (27), together with (28), is a function of the opening ratio only, not affected by the Reynolds number. The reader is referred to Xu et al. (2016) and Xu and Huang (2019) for a comparison of the values of C_f predicted by Eqs. (27) and (28), obtained from the experiment, and simulated by using the orifice-flow method.

For Reynolds number $Re > 100$ and the opening ratio $\alpha < 10\%$, these two formulas give almost the same result. For typical OWCs in a laboratory setting, $Re > O(10^3)$ and $\alpha = O(1\%)$. Therefore, both formulas can give about the same C_f for scaled and full-scale models of OWC WECs with quadratic PTOs. The reader is referred to Appendix A for details.

3.4. Sensitivity of the simulated pneumatic efficiency to the Forchheimer coefficient f

The Forchheimer coefficient f is determined by Eq. (24). Therefore, the sensitivity to f is basically the sensitivity to the quadratic loss coefficient C_f because the numerical results are not sensitive to the thickness of the Forchheimer-flow region as discussed in Section 3.5.

When using an empirical formula such as Eq. (26) or (27) to estimate the quadratic loss coefficient C_f for a given opening ratio, certain uncertainty in the estimated C_f can be expected due to factors such as (1) the treatment of the orifice edges, (2) the measurement error in the opening ratio, and (3) the suitability of the formula for non-standard orifice plates. When C_f is determined by Eq. (18) using the measured pressure and surface elevation, the determination of cross-sectional average velocity becomes a challenge for 3D OWCs. Most existing studied only used one wave gauge to determine the surface elevation inside the OWC chamber and obtained the velocity by taking the time derivative of the surface elevation, and used this velocity to approximate the cross-sectional average velocity; this approach may introduce an error to the value of C_f determined by using Eq. (18), especially when the surface non-uniformity inside the OWC chamber cannot be ignored (Xu and Huang, 2019). This means that even the C_f values obtained from the scaled model tests on OWCs may contain errors (Xu et al., 2016; Xu and Huang, 2019).

The sensitivity of an OWC's pneumatic efficiency ϵ to the uncertainty in C_f, the parameter describing the characteristics of a quadratic PTO, depends on whether or not the PTO has been optimized for the OWC to certain extent: if the PTO has been optimized for the OWC, then $\partial\epsilon/\partial C_f = 0$ at the optimal C_f; in this case, the pneumatic efficiency ϵ is not sensitive to the uncertainty in C_f. However, if the PTO has not been optimized, then the sensitivity of the OWC's pneumatic efficiency ϵ to C_f depends crucially on how far the value of C_f is away from the optimal value. Take the circular OWC studied here for example, the cross-sectional average velocity can be estimated by $\langle w \rangle = O(2\pi A_I/T_w)$, where A_I is the incident wave amplitude and T_w is wave period. If we take $T_w = 1.0\,\mathrm{s}$, A_I=0.02 m, and D=0.125 m, we have $Re = 15700$. Therefore, Eq. (26) or (27) give the same C_f. The measured opening ratio has an uncertainty introduced when fabricating the model. The opening ratio obtained from measuring both the opening and the chamber along several directions is $\alpha = 0.0125 \pm 0.00045$, as a result the values of C_f estimated by either Eq. (26) or (27) is in the range of 15,565 and 17,992 with a mean of $16,713$. The uncertainty in the C_f value obtained using Eq. (27) is about 7.6% relative to the mean. For $T = 1.2$ s, Xu et al. (2016) obtained $C_f \sim 14,000$ based on the surface elevation measured at one location inside the OWC chamber. The orifice opening was not optimized for the circular OWC simulated in this study. From our simulation results obtained using C_f=14,000, 17,000, and 20,000 as inputs to the artificial Forchheimer-flow method, we have $\partial\epsilon/\partial C_f \approx 6.7 \times 10^{-6}$ at $C_f = 16,713$. The simulated pneumatic efficiency at 17,000 is about 0.19, while the values of C_f and ϵ

measured in the experiment are 140,000 and 0.18, respectively, meaning that using Eq. (27) to estimate C_f and compute the pneumatic efficiency may give about 7.0 % uncertainty in the simulated pneumatic efficiency compared to the measurement. In consideration of all possible uncertainties in physical model tests and numerical errors in numerical simulations of orifice flows with very small opening ratios, this uncertainty should be acceptable for practical purposes, especially for OWCs with non-rectangular shapes for which accurate measurement of the pneumatic efficiency is difficult due to the non-uniformity of the water surface inside the OWC chamber.

For narrow slots, He and Huang (2017) has found that both the period of the oscillatory flow and the thickness of the orifice plate affect the C_f value. Presently, there is no existing expression for C_f that can provide a reliable estimation of C_f for narrow slots other than those studied by He and Huang (2017).

It is remarked that the existing expressions for C_f discussed here were initially proposed not for orifice plates used in OWC model tests. The expressions were obtained for either surface waves through perforated/slotted barriers or the steady flow through a standard orifice used for flow control in a pipe. However, the orifices used in the studies of OWCs are not standard orifices and involve oscillatory air flows. Even though several studies in the literature have shown that these expressions for C_f can provided a reasonable estimate of C_f for a given opening ratio (Xu et al., 2016; He and Huang, 2017), it is desirable to have a systematic evaluation of the uncertainty in the estimated values of C_f for problems that have not been studied in the literature. Using the orifice-flow method to simulate 3D OWC problems with orifice plates as PTOs can be a very time-consuming task if the opening ratio is very small: very fine grids are needed in the vicinity of the orifice and very small time steps are needed because the velocity of the air flow through the orifice is very high. Therefore, there is a need to establish an accurate relationship between C_f and the opening ratio through laboratory tests of OWCs.

3.5. Effects of the thickness of the artificial Forchheimer-flow region

In numerical simulations, $h_{lyr} = N_p \Delta z$, where N_p is the number of the grids in the artificial Forchheimer-flow region and Δy is the grid size across the region. Because Forchheimer coefficient f is calculated from the value of

C_f specified by the user,

$$f = \frac{C_f}{N_p \Delta y}, \tag{29}$$

a larger Δy may result in a larger error in the numerical thickness of the artificial Forchheimer-flow region, which can be translated into a larger error in the Forchheimer coefficient f for a given C_f. As long as Δy is reasonably small relative to the thickness h_{lyr}, the numerical results are not sensitive to the thickness of h_{lyr}. To demonstrate this, two values of h_{lyr} were examined for the circular OWC using the same G_2 grid: 0.05 and 0.1m; the values of the pneumatic efficiency obtained using these two thicknesses are 0.1729, 0.1733, respectively.

4. Discussion

4.1. Unimportance of the acceleration and Reynolds stress in the artificial Forchheimer flow

It has been assumed that the acceleration of the artificial Forchheimer flow is not important. This assumption can be verified by the following order-of-magnitude estimation. The ratio of the inertia force to the Forchheimer resistance in Eq. (23) is

$$\frac{\rho \partial \langle w \rangle / \partial t}{0.5 \rho f |\langle w \rangle| \langle w \rangle} = O\left(\frac{2\omega h_{lyr}}{C_f \langle w \rangle}\right) = O\left(\frac{2h_{lyr}}{C_f A_I}\right), \tag{30}$$

where the order-of-magnitude estimation $\langle w \rangle = O(\omega A_I)$, with A_I being the amplitude of the incident waves, has been used. In the experimental study of Xu et al. (2016), $A_I = O(0.05\,\mathrm{m})$, $\alpha = O(0.01)$, and $C_f = O(1.6 \times 10^4)$ according to Eq. (26). Therefore, as long as the thickness of the artificial Forchheimer-flow region $h_{lyr}/A_I \ll O(10^4)$, the local acceleration is not important. This means that theoretically speaking, the inertia coefficient L_α in Eq. (24), which is equal to the thickness of the artificial Forchheimer-flow region, can be set to any reasonable value.

It has been assumed that Reynolds stress is not important in the artificial Forchheimer-flow region. The ratio of the Reynolds stress to the Forchheimer resistance can be estimated by

$$\beta_\mu = \frac{\mu_t U / h_{lyr}}{f U^2} = \frac{\mu_t}{f h_{lyr} U} = \frac{\mu_t}{C_f \omega A_i} \tag{31}$$

where $U = \omega A_i$ is the scale of $\vec{u}$ in the artificial Forchheimer-flow region. Numerical simulations have found that $\mu_t = O(10^{-4}\mathrm{Ns/m^2})$ in the artificial Forchheimer flow region. Take $C_f = 14,000$ and $A_i = 0.02\,\mathrm{m}$, and ω=6.28 rad/s, Eq. (31) gives $\beta_\mu = 5.7 \times 10^{-7}$, which means that the Reynolds stress is not important in the artificial Forchheimer-flow region.

4.2. The minor difference in the flow fields of the water motion obtained by the orifice-flow and artificial Forchheimer-flow methods

Even though these two methods give very different velocity fields of the air flow, they give approximately the same mass flow rate through the PTO and the same air pressure inside the air chamber. As a result, the pneumatic efficiencies obtained by these two methods are close to each other.

The velocity field inside the air chamber can affect the water flow inside the OWC chamber through the kinematic and dynamic boundary conditions at the air-water interface inside the OWC chamber. Assuming that the effects of the non-linearity and viscosity are small in the problem, the flow of the water inside the OWC chamber can be theoretically decomposed into (i) diffracted waves and (ii) radiated waves. The radiated waves are generated by specified conditions on the air-water interface in the absence of the incident waves, while the diffracted waves are generated by the incident waves in the absence of the mechanisms generating the radiated waves. The radiated waves are generated mainly by the fluctuating pressure acting on the air-water interface but slightly affected by the shear stress and velocity of the air flow on the air-water interface.

The following two factors have contributed to the difference in the two velocity fields:

1. A constant C_f is used in the artificial Forchheimer-flow method. The inhalation process of the air flow is not the exactly same as the exhalation process, which makes the C_f for each process slightly different, as argued in the Appendix A. The artificial Forchheimer-flow method uses the averaged value of C_f, which may slightly affect the air pressure during both the inhalation and exhalation periods, and thus make the radiated waves obtained by these two methods slightly different.
2. In addition to the effect of the air pressure, which affect directly the radiated waves, the differences in the air-flow velocity and shear stress at the air-water interface may also slight affect the velocity field of the water motion. However, these effects are expected to be small, thanks to the large difference between the densities of the air and water.

4.3. Unimportance of air compressibility for small OWC models

The compressibility of the air in the OWC chamber and through the PTO is not considered by the current two-phase flow model: (1) when using an orifice as the PTO of an OWC, the air compressibility is neglected, and (2) the influence of the compressibility of the air inside the air chamber is negligible when the height of the air chamber is small.

The compressibility of the air inside the air chamber can cause a difference between the mass flow rate of the air flow close to the air-water interface Q_m and the the mass flow rate through the orifice q_m. As shown in Appendix C, the amplitude ratio of q_m to Q_m can be estimated by

$$\left|\frac{q_0}{Q_0}\right| \approx \frac{1}{\sqrt{1+\epsilon_{ch}^2}}, \epsilon_c = \left(\frac{4C_f C_a}{3\pi}\right)\frac{\omega^2 A_I h_{ch}}{c_a^2} \tag{32}$$

where Q_0 and q_0 are the complex amplitudes of Q_m an q_m, respectively, ω is the wave angular frequency, h_{ch} is the height of the air chamber, c_a is the speed of sound in air, C_a is the amplification factor defined by Eq. (25), and A_I is the amplitude of the incident waves. We can take $c_a = 330$ m/s and $C_a = 1$ for a first-cut estimation of $|q_0/Q_0|$.

For the circular OWC, h_{ch}=0.05 m, $C_f = 1.4 \times 10^4$, ω=O(5 s^{-1}) and $A_I =$ O(0.02 m); Eq. (32) gives $\epsilon_c = O(10^{-3})$. For the rectangular OWC, $h_{ch} =$ 0.30 m, ω=O(5 s^{-1}), $A_I =$ O(0.02 m), and C_f = 68,275, 16,938 and 7,470 for α=0.625%, 1.25% and 1.875%, respectively; Eq. (32) gives $\epsilon_c < O(0.05)$ for all three opening ratios. Therefore, $|q_0/Q_0| \approx 1.0$ for both OWCs studied here, which means the influence of the compressibility of the air inside the air chamber can be ignored for both OWCs studied here. However, for very small opening ratios and much higher air chambers, it is possible that the air compressibility needs to be considered. For a discussion on the scaling of air compressibility, the reader is referred to Dimakopoulos et al. (2017).

5. Conclusions

Air-water two-phase flow simulations of two OWC-type WECs with quadratic PTOs were performed using two methods to model the PTOs: the orifice-flow method and the artificial Forchheimer-flow method. The artificial Forchheimer-flow method was validated by comparing with experimental results and the numerical results obtained by the orifice-flow method. The Forchheimer coefficient can be determined by a given quadratic loss coefficient of the PTO divided by the thickness of the artificial Forchheimer-flow region. For practical purpose, a single Forchheimer coefficient can be used for both the air inhalation and exhalation processes. As long as the thickness of the artificial Forchheimer-flow region (or the thickness of the orifice plate) is not a hundred times larger than the amplitude of the waves, both the acceleration of the artificial Forchheimer flow and the thickness of the region are not important. Even though the two methods for modeling the quadratic PTOs give very different patterns of the air flow, the pneumatic efficiencies obtained using these two methods are very close to each other. The velocity fields of the water flow obtained by the two methods are approximately the same, especially the instantaneous and mean velocity fields near the bed, which are important for local scour around bottom-sitting OWCs. The artificial Forchheimer-flow method can speed up the simulation for at least 25 times. As long as the quadratic loss coefficient is accurate, the pneumatic efficiency obtained using the artificial Forchheimer-flow method is as reliable as that obtained using the orifice-flow method. Since the orifice plates used in OWC studies are not standard ones, there is a need to establish an accurate relationship between the quadratic loss coefficient and the opening ratio for them by laboratory tests of OWCs.

6. Data Availability Statement

The datasets generated and/or analysed during the current study are available from the corresponding author on reasonable request.

7. Acknowledgement

This work was supported by the US National Science Foundation under grant number CBET-1706938 and the Extreme Science and Engineering Discovery Environment (XSEDE) under grant numbers OCE170015 and ENG180008. XSEDE is supported by National Science Foundation grant number ACI-1548562. Any opinions, findings, and conclusions or recommendations expressed in this material are those of the author(s) and do not necessarily reflect the views of the National Science Foundation. This is SOEST contribution No. 11777.

Appendices

A. Expression for C_f based on drag coefficient

As shown in Fig. 7, the air inhalation and exhalation processes are not exactly the same. This is because there is no lateral boundary to bound the air flow on the outflow side of the orifice plate during the air exhalation period, implying that the pressure drop during the air exhalation process and the pressure drop during the air inhalation process may not be exactly the same.

To derive an expression for the quadratic pressure loss coefficient C_f, let's define three horizontal surfaces located $y = y_-$, $y = y_+$, and $y = y_c$, as shown in Fig. A.1. The *vena contracta* is located at $y = y_c$. The distance between y_- and y_+ is scaled by the thickness of the orifice plate. The actual locations of $y = y_-$ and $y = y_+$ should be defined in consideration of the size of the vertices generated on both sides of the orifice plate.

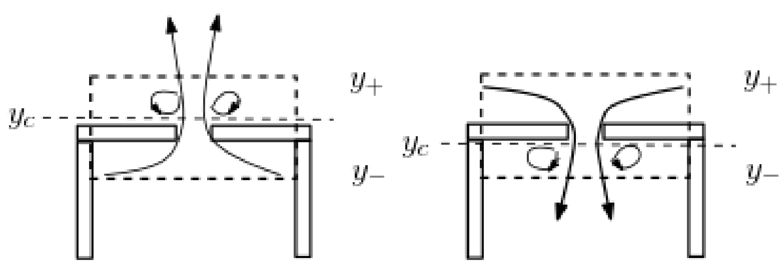

Figure A.1: Oscillatory air flow through an orifice. Left panel: the air exhalation process; right panel: the air inhalation process.

Due to the high speed and small diameter of the circular jet flow, the pressure across the jet flow of the air is approximately uniform, as shown in Fig. 9. The pressure on the inflow side of the orifice plate is also approximately uniform.

During the exhalation period, the vertical velocity of the air flow through the orifice is positive and the air pressure inside the air chamber is larger than the air pressure outside the chamber. The force acting on the orifice plate can be parameterized by the following Morison equation

$$\int\int \Delta p dA = C_D(S - S_o)\frac{1}{2}\rho|w_g|w_g + C_M\rho(S - S_o)L_\delta\frac{\partial w_g}{\partial t}, \qquad \text{(A.1)}$$

where the integration is over the surface of the orifice plate, w_g is the velocity of the air flow in the opening, $\Delta p = \tilde{p}_{in} - \tilde{p}_{out}$ with $\tilde{p}_{in}$ and $\tilde{p}_{out}$ being the dynamic pressures inside and outside the air chamber, respectively, S_o is the area of the orifice, S is the cross-sectional area of the air chamber, C_D is a drag coefficient and C_M is an added mass coefficient. Both C_M and C_D can be functions of the opening ratio α and the Reynolds number.

The fact that the air pressure is approximately uniform on either side of the orifice plate allows for the following approximation to Eq. (A.1):

$$\tilde{p}_{in} - \tilde{p}_{out} = C_D \frac{1}{2} \rho w_g^2 + C_M \rho L_\delta \frac{\partial w_g}{\partial t}. \tag{A.2}$$

Let the cross-sectional average velocity of the air inside the air chamber be $\langle w \rangle$, the conservation of mass for the in-compressible air gives

$$S\langle w \rangle = S_o w_g, \text{ or } \langle w \rangle = \alpha w_g. \tag{A.3}$$

Therefore, Eq. (A.2) can be further written as

$$\tilde{p}_{in} - \tilde{p}_{out} = \frac{1}{2} C_f \rho \langle w \rangle^2 + L_\alpha \rho \frac{\partial \langle w \rangle}{\partial t}, \tag{A.4}$$

where

$$C_f = \frac{C_D}{\alpha^2}, \quad L_\alpha = C_M \frac{L_\delta}{\alpha} \tag{A.5}$$

During the air inhalation period, the vertical velocity of the air flow through the orifice is negative and the air pressure in the air chamber is smaller than the air pressure outside the air chamber. Similar to the exhalation period, the pressure drop during the inhalation period can be parameterized by

$$\tilde{p}_{out} - \tilde{p}_{in} = \frac{1}{2} C_f \rho \langle w \rangle^2 - L_\alpha \rho \frac{\partial \langle w \rangle}{\partial t}. \tag{A.6}$$

Because the velocity is negative during the air inhalation period, $\langle w \rangle = -|\langle w \rangle|$. It then follows that Eq. (A.6) can be rewritten as

$$\tilde{p}_{in} - \tilde{p}_{out} = \frac{1}{2} C_f \rho |\langle w \rangle| \langle w \rangle + \rho L_\alpha \frac{\partial \langle w \rangle}{\partial t}. \tag{A.7}$$

Since $\langle w \rangle > 0$ during the exhalation period, Eq.(A.7) is the same as Eq. (A.4). Therefore, Eq.(A.7) can be used for both the exhalation and inhalation periods, with the understanding that the inhalation and exhalation periods should have different values of C_f and L_α . Furthermore, effects of Reynolds number on C_f and L_α are expected due to their dependence on the drag and inertia coefficients of the orifice plate.

The relative importance of the inertia term to the drag term can be estimated by the ratio of these two terms.

$$\frac{L_\alpha \rho \partial \langle w \rangle / \partial t}{0.5 C_f \rho |\langle w \rangle| \langle w \rangle} = O\left(\frac{2L_\alpha}{C_f A_I}\right) = O\left(\frac{C_M}{C_D}\frac{2\alpha L_\delta}{A_I}\right), \tag{A.8}$$

which $\langle w \rangle = O(\omega A_I)$ and $\partial/\partial t = O(\omega)$ have been used. Normally $C_D = O(1)$ and $C_M = O(1)$. If we take $C_D/C_M = O(1)$ and $A_I = O(2L_\delta)$, the ratio of the inertia term to the drag term is on the order of the opening ratio α, which is normally about 0.01 for typical OWC problems.

Using different values of C_f for the air inhalation and exhalation periods to fit the experimental data of Xu et al. (2016), the following has been found: (1) the C_f value for the exhalation period is slightly smaller than that for the inhalation period; (2) the average of the C_f-values for the air inhalation and exhalation periods is close to the value obtained by fitting Eq. (18) to the measured pressure with a single C_f, and (3) the two values of C_f deviate from their mean by about 7%. For practical purposes, the effects of the air inhalation and exhalation periods on C_f can be ignored and a single C_f can be used to model the pressure drop across an orifice.

If the inertia term and the effects of air inhalation and exhalation process can be neglected, Eq.(A.7) can be approximated by

$$\tilde{p}_{in} - \tilde{p}_{out} = \frac{1}{2} C_f \rho |\langle w \rangle| \langle w \rangle. \tag{A.9}$$

Therefore, the quadratic loss coefficient C_f can be determined by the resistance coefficient for a thin orifice in a pipe as if the flow is steady; this makes it possible to estimate C_f using the resistance coefficient of Crane (1957) for a steady in-compressible flow through a thin orifice in a pipe,

Mei (1992) studied the loss of hydrostatic pressure induced by long water waves through a vertical perforated plate, and derived an expression for the pressure drop similar to Eq. (A.7) and obtained an expression for C_f, which is a function of the flow contraction coefficient C_c. For long water waves through a vertical perforated plate, C_f is the same for both the forward and backward flows. Mei (1992) also argued that the inertia term is not important compared to the quadratic loss term. For the oscillatory air flow through a circular sharp-edged orifice, Xu et al. (2016) and He and Huang (2017) have found that the well-known Chisholm expression for C_c (Fossa and Guglielmini, 2002) can provide a good estimation of C_c for OWC problems.

B. Mesh convergence study

The mesh dependence study has been done in three steps: (i) the mesh configuration for the empty wave flume, (ii) the local mesh configuration for simulating the OWC model using the orifice-flow method, and (iii) the local mesh configuration for simulating the OWC model using the artificial Forchheimer-flow method.

(i) Huang et al. (2020) has shown that at the location where the OWC model to be installed, the mesh configuration for the empty flume can produce the surface elevation in a very good agreement with the theoretical result for second order Stokes waves.

(ii) In simulating OWCs using the orifice-flow method, a finer grid is needed to resolve the flow through the orifice. For the mesh configuration in the vicinity of the orifice, Xu and Huang (2019) examined three sets of mesh configurations in the vicinity of the orifice generated by using OepnFOAM's built-in *SnappyHexMesh* utility: a coarser mesh: 1.5 mm x 1.5 mm x 1.5 mm; the a medium mesh: 1.0 mm x 1.0 mm x 1.0 mm; and a finer mesh: 0.5 mm x 0.5 mm x 0.5 mm. The *snappyHexMesh* utility takes an already existing mesh and automatically generates refined 3-dimensional meshes containing hexahedra and split-hexahedra from triangulated surface geometries of a model. Xu and Huang (2019) used two intermediate meshes between the meshes for the empty flume and the meshes generated by *snappyHexMesh* to provide a smooth transition, and showed that the quadratic loss coefficients obtained using the medium mesh had less than 3% difference from those obtained using the finer mesh. A mesh of $0.001\,25\,\mathrm{m} \times 0.001\,25\,\mathrm{m} \times 0.001\,25\,\mathrm{m}$ was adopted here to achieve a balance between computational cost and accuracy.

(iii) For the local mesh configuration used in the artificial Forchheimer flow method, another set of simulation was performed for the circular OWC with T =1.2 s by reducing the current G_2 mesh by 60%. The refined mesh only reduces the pneumatic efficiency by 4.75%. The present mesh was chosen to achieve a balance between computational cost and accuracy.

C. Calculation of mass flux through the orifice

We consider a typical OWC air chamber. The instantaneous volume of this air chamber is V and the mass of the air inside this air chamber is $m = \rho V$, where ρ is the instantaneous density of the air inside the air chamber. The mass flux through the orifice S_0 is the time rate of change of m

$$q_m = \frac{dm}{dt} = \frac{d}{dt}(\rho V). \tag{C.1}$$

The instantaneous volume V can be written as the sum of its initial volume of the air chamber V_0 and the change due to the surface displacement η

$$V = V_0 + \int\int \eta dA, \tag{C.2}$$

where $V_0 = Sh_{ch}$ with S and h_{ch} being the cross-sectional area and initial height of the air chamber, respectively. It then follows that

$$q_m = (V_0 + \langle\eta\rangle S)\frac{d\rho}{dt} + \rho S\frac{d\langle\eta\rangle}{dt}, \quad \langle\eta\rangle = \frac{1}{S}\int\int \eta dA, \tag{C.3}$$

where $\langle\eta\rangle$ is the cross-sectional average of η inside the OWC chamber. Physically, $q_m = dm/dt$ is the mass flux at the orifice and $Q_m = \rho S d\langle\eta\rangle/dt$ is the mass flux at the air-water interface. The difference between q_m and Q_m is due to the compressiblility of the air in the air chamber.

For compressible air, let $\rho = \rho_0 + \rho'$ with ρ' being the change of air density due to a change in pressure. We have from Eq. (C.3)

$$\frac{dm}{dt} = (V_0 + \langle\eta\rangle S)\frac{d\rho'}{dt} + (\rho_0 + \rho')S\frac{d\langle\eta\rangle}{dt}. \tag{C.4}$$

For compressible air, the mass fluxes through different cross sections are different. Assuming $\rho' \ll \rho_0$ and $S\langle\eta\rangle \ll V_0$, Eq. (C.4) can be linearized to give

$$q_m \approx V_0\frac{d\rho'}{dt} + Q_m, \quad Q_m = \rho_0 S\frac{d\langle\eta\rangle}{dt} \tag{C.5}$$

For ideal gas and an isentropic process

$$\frac{dp}{d\rho} = c_a^2 \tag{C.6}$$

where c_a is the sound speed in air. It then follows from Eq. (C.6) that

$$\frac{d\rho'}{dt} = \frac{1}{c_a^2}\frac{dp}{dt} \tag{C.7}$$

Using Eq. (C.7) in Eq. (C.5) gives

$$q_m = \frac{V_0}{c_a^2}\frac{dp}{dt} + Q_m \tag{C.8}$$

According to Eq. (18), the pressure drop across the orifice plate is quadratically related to cross-sectional average of the velocity w,

$$p = \frac{1}{2}C_f\rho|\langle w\rangle|\langle w\rangle, \tag{C.9}$$

Xu et al. (2016) has showed that the quadratic pressure drop can be linearized as

$$p = \rho_0 C_e\langle w\rangle \equiv C_e q_m/S, \tag{C.10}$$

and the linear coefficient C_e is related to the quadratic loss coefficient C_f by

$$C_e = \frac{C_f}{2}\frac{8}{3\pi}|U_0| \tag{C.11}$$

where $|U_0|$ is the amplitude of the oscillatory velocity of the air flow in the air chamber. In terms of the amplification factor C_a, $U_0 = C_a\omega A_I$ with A_I and ω being the amplitude and angular frequency of the incident waves, respectively, which means that Eq. (C.11) can be rewritten as

$$C_e = \frac{4}{3\pi}C_f C_a\omega A_i. \tag{C.12}$$

Assuming sinusoidal variations of Q_m and q_m and using Eqs. (C.10)-(C.12), we can obtain from Eq. (C.8),

$$\left|\frac{q_0}{Q_0}\right| \approx \frac{1}{\sqrt{1+\epsilon_{ch}^2}}, \quad \epsilon_c = \frac{\omega C_e h_{ch}}{c_a^2} = \left(\frac{4C_f C_a}{3\pi}\right)\frac{\omega^2 A_i h_{ch}}{c_a^2} \tag{C.13}$$

where Q_0 and q_0 are the complex amplitudes of Q_m and q_m.

It is remarked that, Dimakopoulos et al. (2015) expressed ϵ_c as

$$\epsilon_c = \frac{\omega K h_{ch}}{\gamma p_{atm}} \tag{C.14}$$

where K is a linear damping coefficient, $p_{atm} = 10^5$ Pa is the atmospheric pressure and $\gamma = 1.4$ for ideal gas. Eq. (C.14) can be obtained from Eq. (C.13) if we use $c_a^2 = \gamma p_{atm}/\rho_0$ for perfect gas and take $K = \rho_0 C_e$. Dimakopoulos et al. (2015) used Eq. (C.14) to discuss the effect of air compressibility in a long pipe with an orifice, which was used as the PTO in the experiment they studied.

References

Aderinto, T., Li, H., 2018. Ocean wave energy converters: Status and challenges. Energies 11, 1250.

Ahmad, N., Bihs, H., Myrhaug, D., Kamath, A., Arntsen, Ø.A., 2018. Three-dimensional numerical modelling of wave-induced scour around piles in a side-by-side arrangement. Coastal Engineering 138, 132–151.

Anbarsooz, M., Faramarzi, A., 2016. A numerical study on the performance of fixed oscillating water column wave energy converter at steep waves, in: Proceedings of the ASME 2016 Power Conference(POWER2016).

Badhurshah, R., Dudhgaonkar, P., Jalihal, P., Samad, A., 2018. High efficiency design of an impulse turbine used in oscillating water column to harvest wave energy. Renewable Energy 121, 344–354.

Çelik, A., Altunkaynak, A., 2020. Determination of hydrodynamic parameters of a fixed owc by performing experimental and numerical free decay tests. Ocean Engineering , 106827.

Chen, Z., Yu, H., Hu, M., Meng, G., Wen, C., 2013. A review of offshore wave energy extraction system. Advances in Mechanical Engineering 5, 623020.

Courant, R., Friedrichs, K., Lewy, H., 1967. On the partial difference equations of mathematical physics. IBM Journal of Research and Development 11, 215–234.

Crane, C., 1957. Flow of fluids through valves, fittings, and pipe [Technical Paper No. 410]. Crane Company Engineering Division, Chicago.

Delauré, Y., Lewis, A., 2003. 3d hydrodynamic modelling of fixed oscillating water column wave power plant by a boundary element methods. Ocean Engineering 30, 309 – 330.

Deng, Z., Huang, Z., Law, A.W., 2013. Wave power extraction by an axisymmetric oscillating-water-column converter supported by a coaxial tube-sector-shaped structure. Applied Ocean Research 42, 114 – 123.

Dimakopoulos, A., Cooker, M., Medina-Lopez, E., Longo, D., 2015. Flow characterisation and numerical modelling of owc wave energy converters, in: EWTEC 2015 (12th European Wave and Tidal Energy Conference 2015).

Dimakopoulos, A.S., Cooker, M.J., Bruce, T., 2017. The influence of scale on the air flow and pressure in the modelling of oscillating water column wave energy converters. International Journal of Marine Energy 19, 272 – 291.

Elhanafi, A., Macfarlane, G., Fleming, A., Leong, Z., 2017. Investigations on 3D effects and correlation between wave height and lip submergence of an offshore stationary owc wave energy converter. Applied Ocean Research 64, 203–216.

Falcão, A.F.d.O., 2010. Wave energy utilization: A review of the technologies. Renewable and Sustainable Energy Reviews 14, 899 – 918.

Fossa, M., Guglielmini, G., 2002. Pressure drop and void fraction profiles during horizontal flow through thin and thick orifices. Experimental Thermal and Fluid Science 26, 513 – 523.

Galera-Calero, L., Blanco, J.M., Izquierdo, U., Esteban, G.A., 2020. Performance assessment of three turbulence models validated through an experimental wave flume under different scenarios of wave generation. Journal of Marine Science and Engineering 8, 881.

Gurnari, L., Filianoti, P.G., Torresi, M., Camporeale, S.M., 2020. The wave-to-wire energy conversion process for a fixed u-owc device. Energies 13, 283.

He, F., Huang, Z., 2017. Characteristics of orifices for modeling nonlinear power take-off in wave-flume tests of oscillating water column devices. Journal of Zhejiang University-SCIENCE A 18, 329–345. doi:10.1631/jzus.A1600769.

He, F., Huang, Z., Wing-Keung Law, A., 2012. Hydrodynamic performance of a rectangular floating breakwater with and without pneumatic chambers: An experimental study. Ocean Engineering 51, 16 – 27.

Huang, Z., Huang, S., Xu, C., 2020. Characteristics of the flow around a circular owc-type wave energy converter supported by a bottom-sitting c-shaped structure. Applied Ocean Research 101, 102228.

Huang, Z., Xu, C., Huang, S., 2019. A CFD simulation of wave loads on a pile-type oscillating-water-column device. Journal of Hydrodynamics 31, 41–49.

Jacobsen, N.G., Fuhrman, D.R., Fredsöe, J., 2012. A wave generation toolbox for the open-source CFD library: OpenFoam. International Journal for Numerical Methods in Fluids 70, 1073–1088.

Kalitzin, G., Medic, G., Iaccarino, G., Durbin, P., 2005. Near-wall behavior of rans turbulence models and implications for wall functions. Journal of Computational Physics 204, 265–291.

Kamath, A., Bihs, H., Arntsen, Ø.A., 2015a. Numerical investigations of the hydrodynamics of an oscillating water column device. Ocean Engineering 102, 40–50.

Kamath, A., Bihs, H., Arntsen, Ø.A., 2015b. Numerical modeling of power take-off damping in an oscillating water column device. International Journal of Marine Energy 10, 1–16.

Larsen, B.E., Fuhrman, D.R., 2018. On the over-production of turbulence beneath surface waves in reynolds-averaged navier–stokes models. Journal of Fluid Mechanics 853, 419–460.

Liu, Z., Hyun, B., Jin, J., Hong, K., Lee, Y., 2016. OWC air chamber performance prediction under impulse turbine damping effects. Science China Technological Sciences 59. doi:10.1007/s11431-016-6030-5.

López, I., Castro, A., Iglesias, G., 2015. Hydrodynamic performance of an oscillating water column wave energy converter by means of particle imaging velocimetry. Energy 83, 89 – 103.

López, I., Pereiras, B., Castro, F., Iglesias, G., 2014. Optimisation of turbine-induced damping for an owc wave energy converter using a RANS–VOF numerical model. Applied Energy 127, 105–114.

Lund, H., 2007. Renewable energy strategies for sustainable development. Energy 32, 912–919.

Luo, Y., Nader, J.R., Cooper, P., Zhu, S.P., 2014. Nonlinear 2d analysis of the efficiency of fixed oscillating water column wave energy converters. Renewable Energy 64, 255 – 265.

Mahnamfar, F., Altunkaynak, A., 2017. Comparison of numerical and experimental analyses for optimizing the geometry of OWC systems. Ocean Engineering 130, 10 – 24.

Martins-Rivas, H., Mei, C.C., 2009. Wave power extraction from an oscillating water column at the tip of a breakwater. Journal of Fluid Mechanics 626, 395–414.

Mei, C.C., 1992. The Applied Dynamics of Ocean Surface Waves. World Scientific.

Menter, F.R., 1994. Two-equation eddy-viscosity turbulence models for engineering applications. AIAA journal 32, 1598–1605.

Morris-Thomas, M.T., Irvin, R.J., Thiagarajan, K.P., 2007. An investigation into the hydrodynamic efficiency of an oscillating water column. J. Offshore Mech. Arct. Eng. 129, 273–278.

Ning, D.Z., Shi, J., Zou, Q.P., Teng, B., 2015. Investigation of hydrodynamic performance of an owc (oscillating water column) wave energy device using a fully nonlinear HOBEM (higher-order boundary element method). Energy 83, 177 – 188.

Ning, D.Z., Wang, R.Q., Zou, Q.P., Teng, B., 2016. An experimental investigation of hydrodynamics of a fixed owc wave energy converter. Applied Energy 168, 636 – 648.

Rusche, H., 2003. Computational fluid dynamics of dispersed two-phase flows at high phase fractions. Ph.D. thesis. Imperial College London (University of London).

Sarmento, A., 1992. Wave flume experiments on two-dimensional oscillating water column wave energy devices. Experiments in fluids 12, 286–292.

Sarmento, A.J., Falcão, A.d.O., 1985. Wave generation by an oscillating surface-pressure and its application in wave-energy extraction. Journal of Fluid Mechanics 150, 467–485.

Scuotto, M., De, A., Falcao, A., 2005. Wells and impulse turbines in an owc wave power plant: A comparison, in: Proceedings of the 6th European Wave Tidal Energy Conference, pp. 463–469.

Shalby, M., Elhanafi, A., Walker, P., Dorrell, D.G., 2019. Cfd modelling of a small–scale fixed multi–chamber owc device. Applied Ocean Research 88, 37–47.

Simonetti, I., Cappietti, L., Elsafti, H., Oumeraci, H., 2018. Evaluation of air compressibility effects on the performance of fixed owc wave energy converters using cfd modelling. Renewable Energy 119, 741–753.

Vyzikas, T., Deshoulières, S., Barton, M., Giroux, O., Greaves, D., Simmonds, D., 2017. Experimental investigation of different geometries of fixed oscillating water column devices. Renewable Energy 104, 248 – 258.

Wang, D., Katory, M., Li, Y., 2002. Analytical and experimental investigation on the hydrodynamic performance of onshore wave-power devices. Ocean Engineering 29, 871 – 885.

Weller, H., Tabor, G., Jasak, H.and Fureby, C., 1998. A tensorial approach to computational continuum mechanics using object-oriented techniques. Computers in Physics 12, 620 – 1631.

Xu, C., Huang, Z., 2019. Three-dimensional CFD simulation of a circular owc with a nonlinear power-takeoff: Model validation and a discussion on resonant sloshing inside the pneumatic chamber. Ocean Engineering 176, 184 – 198.

Xu, C., Huang, Z., Deng, Z., 2016. Experimental and theoretical study of a cylindrical oscillating water column device with a quadratic power take-off model. Applied Ocean Research 57, 19 – 29.

Zhang, Y., Zou, Q.P., Greaves, D., 2012. Air–water two-phase flow modelling of hydrodynamic performance of an oscillating water column device. Renewable Energy 41, 159 – 170.

Zhao, K., Cheng, N.S., Huang, Z., 2014. Experimental study of free-surface fluctuations in open-channel flow in the presence of periodic cylinder arrays. Journal of Hydraulic Research 52, 465–475.

Zheng, S., Antonini, A., Zhang, Y., Greaves, D., Miles, J., Iglesias, G., 2019. Wave power extraction from multiple oscillating water columns along a straight coast. Journal of Fluid Mechanics 878, 445–480.

Zheng, S., Zhu, G., Simmonds, D., Greaves, D., Iglesias, G., 2020. Wave power extraction from a tubular structure integrated oscillating water column. Renewable Energy 150, 342 – 355.